### Title

Unlocking i-process nucleosynthesis by bridging stellar and nuclear physics




### Journal

Nature Reviews Physics, 7(12)

### ISSN

2522-5820



### Authors

Wiedeking, Mathis

Goriely, Stephane

Guttormsen, Magne

et al.



### Publication Date

2025-12-01

### DOI

10.1038/s42254-025-00885-7

Peer reviewed

# Unlocking intermediate neutron-capture-process nucleosynthesis by bridging stellar astrophysics and nuclear physics

**Mathis Wiedeking[1,*], Stephane Goriely[2], Magne Guttormsen[3,4], Falk Herwig[5], Ann-Cecilie Larsen[3,4], Sean N. Liddick[6,7], Dennis Mücher[8], Andrea L. Richard[9], Sunniva Siem[3,4], and Artemis Spyrou[6,10]**

[1]Nuclear Science Division, Lawrence Berkeley National Laboratory, Berkeley, CA 94720, USA
[*]e-mail: mwiedeking@lbl.gov
[2]Institut d'Astronomie et d'Astrophysique, Université Libre de Bruxelles, Campus de la Plaine CP 226, 1050 Brussels, Belgium
[3]Department of Physics, University of Oslo, NO-0316 Oslo, Norway
[4]Norwegian Nuclear Research Centre, NO-0316 Oslo, Norway
[5]Astronomy Research Centre and Department of Physics and Astronomy, University of Victoria, P.O. Box 3055, STN CSC, Victoria, BC V8W 3P6, Canada
[6]Facility for Rare Isotope Beams, Michigan State University, East Lansing, Michigan 48824, USA
[7]Department of Chemistry, Michigan State University, East Lansing, Michigan 48824, USA
[8]Institute for Nuclear Physics, University of Cologne, 50937 Köln, Germany
[9]Department of Physics and Astronomy, Ohio University, Athens, Ohio 45701, USA
[10]Department of Physics and Astronomy, Michigan State University, East Lansing, Michigan 48824, USA

## ABSTRACT

The origin of chemical elements and their abundances across the cosmos remains one of the central questions in physics. The formation of elements heavier than iron is traditionally attributed to three main mechanisms: the slow and rapid neutron-capture processes ($s$ and $r$ processes) and the $p$ process mostly driven by photodisintegration reactions. However, certain astronomical observations reveal elemental abundance patterns inconsistent with these processes. These prompted the intermediate neutron-capture process ($i$ process), which operates at neutron densities between the $s$ and $r$ processes, to emerge as a key area of research. Observations of elemental abundances of stars confirm that the $i$ process indeed takes place. Identifying the required astrophysical conditions and contributions of the $i$ process sensitively depend on neutron-capture reaction rates involving unstable atomic nuclei. Significant advancements have been achieved due to these new astronomical observations and cutting-edge nuclear physics experimental and analytical techniques, in addition to nuclear physics and nucleosynthesis models. State-of-the-art facilities and theoretical models are revolutionizing our ability to explore the $i$ process and offer fresh perspectives on the nuclear behaviour under extreme stellar conditions. This review underscores the synergy between groundbreaking astronomical and nuclear physics research, bridging nuclear physics and observational astrophysics, and advancing our understanding of $i$-process nucleosynthesis.

## 1 Introduction

One of the fundamental questions in science concerns the origin of the chemical elements we observe in the universe. The elements that make up our planet and solar system are also present in stars, within our Galaxy and beyond. The amounts of the different elements (abundances) change from star to star, showing that there are multiple nucleosynthesis processes at play. The goal, therefore, is to identify and characterize these different processes and their contributions to the galactic enrichment.

In the 1950s, the idea that the elements were mainly produced during the Big Bang was still popular[1] until the first direct observation that heavy elements are presently produced in stars[2]. Studying absorption lines from starlight, the element technetium (Tc) was identified. The longest-lived isotope of Tc has a half-life of four million years. Therefore, if any Tc was produced during the Big Bang it should have been destroyed long ago. Soon after the Tc discovery, a comprehensive description of stellar nucleosynthesis was published in 1957 by Burbidge, Burbidge, Fowler and Hoyle[3] and independently by Cameron[4]. The foundations laid by these publications are, to a large extent, still valid today. However, advancements in modern astronomy, astrophysical modeling and nuclear science have been pushing the scientific community to widen its perspectives as not all

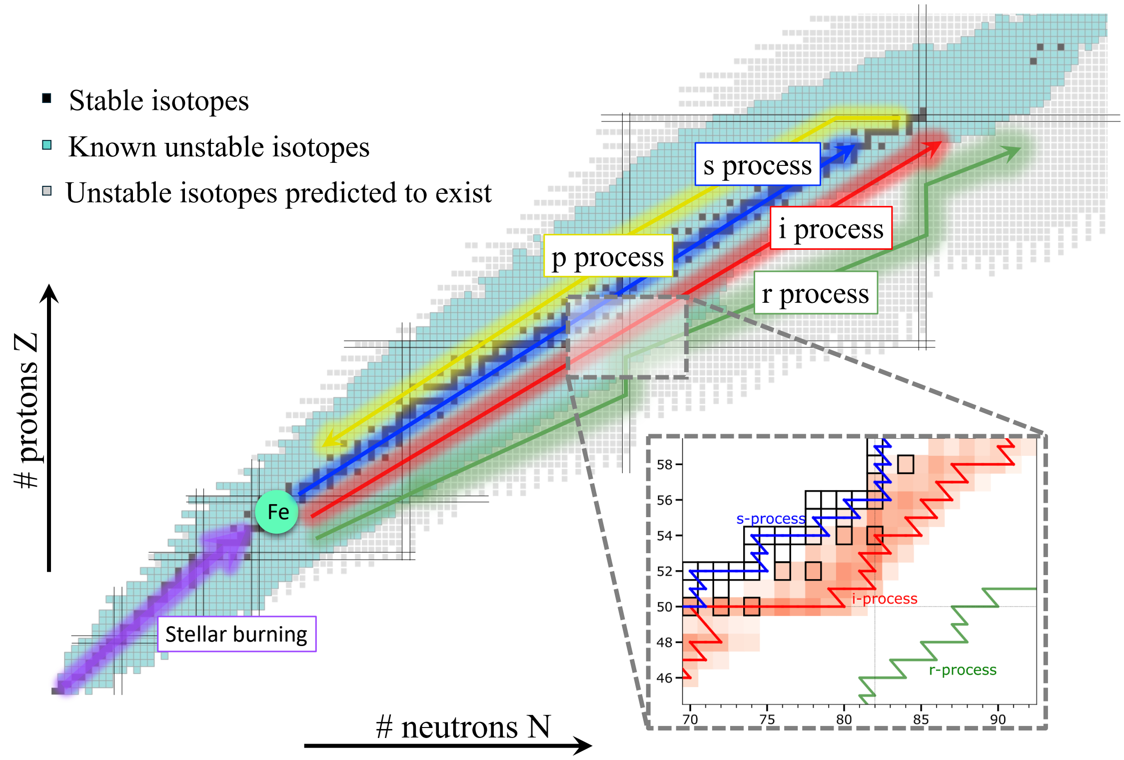


**Figure 1. Chart of Nuclides with Nucleosynthesis Pathways**
Chart of the nuclides with approximate paths for the various nucleosynthesis processes. The $y$ axis corresponds to the number of protons ($Z$) and the $x$ axis to the number of neutrons ($N$). Each square represents a nucleus with a mass number of $A$ composed of a unique combination of protons and neutrons (isotopes of elements). Isotopes that are stable against radioactive decay, are presented as black squares and create the so-called valley of stability. The light-blue squares represent unstable isotopes which have been produced in the laboratory so far, while the gray squares show unstable isotopes that are predicted to exist. The horizontal and vertical solid black lines indicate closed shells for $N$ and $Z$. The inset on the bottom right shows a region of isotopes involved in the *i* process (shaded red squares) as well as a sample *i*-process reaction flow with red lines.

observations can be reconciled with these pioneering descriptions.

Before diving into the modern discoveries, it is useful to summarize the classic nucleosynthesis picture which was, until recently, considered complete. The lightest elements, hydrogen and helium, are mostly produced during the first few minutes of the Big Bang. The elements up to the region of iron, are mainly produced during stellar burning processes (purple line in Fig. 1). The focus of the present review is on the synthesis of elements heavier than iron, which are traditionally attributed to three main processes: the slow ($s$)[5], and rapid ($r$)[6–8] neutron-capture processes, and the $p$ process[9,10] mostly driven by photodisintegration reactions (represented in Fig. 1 by the blue, green and yellow lines, respectively). All three of these processes still have significant uncertainties and unanswered questions, and until recently were considered to be the only contributors to heavy element nucleosynthesis. The picture started to change when new astronomical observations showed elemental abundance patterns that could not be explained by these processes. In this review, we highlight the intermediate ($i$) neutron-capture process (Fig. 1, red line), which can explain some of these unexpected observations. The $i$ process is also driven by neutron-capture reactions and operates between the $s$ ($10^7$ to $10^{12}$ neutrons/cm$^3$) and $r$ ($\gg 10^{21}$neutrons/cm$^3$) processes. An early version of the $i$ process was first introduced in 1977[11], in the context of the production of lighter elements in evolved red giant stars.

The $i$-process nucleosynthesis[12,13] and its astrophysical sites (red giants[14] and central stars of planetary nebulae[15]) were explored[16,17] although the term $i$ process was not used again until it was realized[18] that this new and distinct mode of neutron-capture nucleosynthesis can resolve the puzzle of the anomalous abundances in some carbon-enhanced metal-poor (CEMP) stars[18,19].

In this review, we highlight the astrophysical $i$ process from different perspectives. As for most nuclear astrophysics studies, observations, astrophysical modeling, nuclear physics and nuclear data input need to work in synergy to address the open questions (Fig. 2). We will explore the astronomical sites where the $i$ process may occur, discuss the current theoretical understanding and highlight how measurements of specific nuclear physics properties are essential for refining these models.

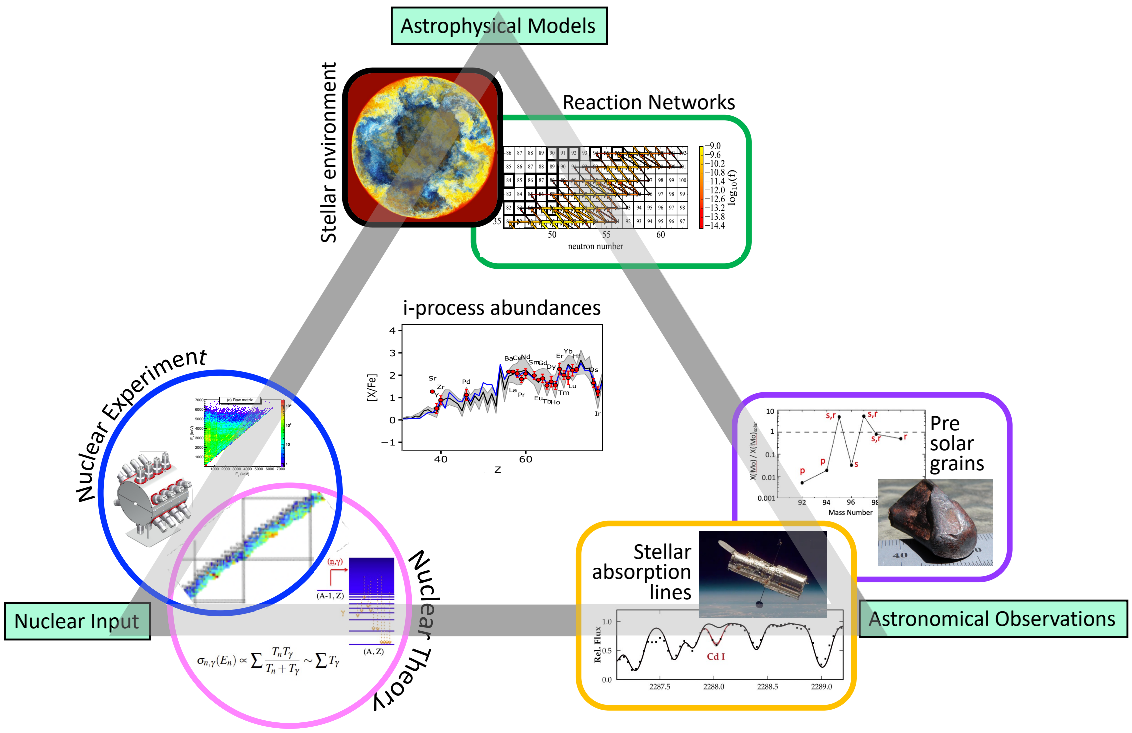


**Figure 2. Interdisciplinary Approach to *i*-Process Research**

Overview of the different fields that work in synergy to address questions on the *i*-process abundances. The bottom-left corner represents the nuclear physics input which is provided by theory and experiment. The astrophysical models of the stellar conditions as well as the nuclear reaction network are shown on the top. The bottom-right corner represents the astronomical observations of *i*-process signatures. Figures, adapted or reproduced with permission from from Refs.[20–24].

## 2 Observational indications of the *i* process

The most prominent impact of the *i* process is in abundance signatures related to trans-iron elements. However, when *i*-process neutron densities are reached, isotopic or abundance signatures of lighter elements can be impacted as well. Observational signatures of the *i* process have been detected across diverse astronomical objects, providing insights into the conditions and astrophysical sites where this nucleosynthesis mechanism operates. Abundance signatures in other objects may likewise reflect *i*-process contributions pending further study.

- CEMP stars: A significant fraction of CEMP stars show abundance patterns that initially appeared to represent a combination of the *s* process and *r* process, showing simultaneous enhancements of, for example, the dominantly *s*-process elements Ba and La, as well as Eu, which is usually attributed to the *r* process. These dual-signature stars were thus classified as CEMP-r/s stars[25]. However, most of them do not show the strong enhancements of the genuine *r*-process elements Os and Ir as expected if their Eu enhancements is the result of *r*-process nucleosynthesis, as shown in detailed observational studies[26,27]. Additional investigations highlighted the challenges in explaining their abundance patterns with traditional nucleosynthesis models[28,29].

- Sakurai's object: This star had left the Asymptotic Giant Branch phase (AGB), the final stage of nuclear burning, and was about to evolve into a white dwarf when it underwent a last very late thermal pulse, exhibiting rapid changes in surface composition. The observed elemental abundances[30], particularly the factor of 100 enhancement compared to the solar abundance of the elements Sr, Y, Zr combined with the absence of enhancement of Ba and La were impossible to explain with *s*-process nucleosynthesis. However, the observations agree well with models of this so-called born-again AGB evolution featuring a short high-intensity neutron burst typical for *i*-process nucleosynthesis models[31].

- Pre-solar grains: Pre-solar meteoritic grains measurements yield isotopic ratios, and the nucleosynthesis signature of the *i* process could be revealed in these ratios. Grains characterized by their low $^{12}C/^{13}C$ ratio show large $^{32}S$ excesses[32]. These isotopic ratios along with the absence of $^{44}Ti$ are consistent with an *i*-process nucleosynthesis in a born-again AGB star like Sakurai's object that would lead to the production of $^{32}Si$ with a half-life long enough to decay after incorporation into SiC grains[33]. Using pre-solar grains to study the *i* process is a promising, complementary approach to be explored in the future.

- AGB, post-AGB stars and subdwarfs: Recent surveys of AGB and post-AGB stars have revealed a subset with abundance patterns consistent with *i*-process nucleosynthesis, suggesting this process may occur more commonly than previously thought in the late stages of low- and intermediate-mass stellar evolution, even at solar-like metallicity[34–38]. Large heavy-element enhancements observed in the related He-rich hot subdwarfs[39], which are the outcomes of stellar mergers, have been linked to the *i* process[40].

- Open clusters: Observations of open clusters[41] have revealed unexpectedly high Ba/La ratios up to four times the ratio expected from either the *s* or *r* process. High Ba/La ratios have been observed in some of the CEMP-r/s stars mentioned above and are theoretically possible in low-*Z* environments[42,43]. However, current simulations do not predict *i*-process enhancements for $A \approx 130$ nuclides at the higher metal content of open-cluster stars, unless ad-hoc assumptions are made.

- Notable individual stars: An incomplete list of individual stars in which *i* process has potentially been detected include the following. The Keller star is the star with the smallest Fe abundance known[44]. Only an upper limit could be determined with at most 3.4 million times less Fe than the Sun. This extremely metal-poor star shows however measured Li, C, Mg and Ca concentration. It has been suggested that Ca in the Keller star could come from *i*-process nucleosynthesis in early generations of massive stars[45]. The metal-poor star HD 94028 shows a ratio of As/Ge ten times larger than in the Sun. This anomalous ratio could not be explained by *s*-process or *r*-process nucleosynthesis, but could be consistent with *i*-process nucleosynthesis pending further experimental investigation[46]. CES0424-1501 is a moderately metal-poor star and was reported as part of a sample of *r*-process-enriched stars[47] and shows large Hf to Ir and Os ratios which is a sign of the *i* process.

- Impact on solar system composition: Stellar population and galactic chemical evolution simulations suggest that the *i* process could contribute to the production of heavy isotopes of elements in the $N$=50 closed neutron-shell peak in the solar system[48]. Current studies have only explored the impact of rapidly accreting white dwarfs, but the *i* process in other astrophysical sites could also contribute to the solar system abundances of these elements.

These diverse observations point to the *i* process as a distinct nucleosynthesis mechanism operating in various stellar environments, potentially at all metallicities.

The classification of the nature of the observed heavy-element stellar enrichment in terms of the different neutron-density regimes for the *s*, *i* or *r* processes is still not fully established and remains ambiguous for CEMP-r/s stars and other classes. The initially proposed indicator[25,49] is related to the [Ba/Eu] or [La/Eu] ratios, reflecting the simultaneous presence of elements like Ba or La predominantly produced by the s-process and Eu by the r-process. Later, a criterion using the relative enhancement of elements near the $N$=50 and $N$=82 closed-neutron shell peaks was proposed[50,51]. However, using such criteria, the boundary between the CEMP-s (dominantly s-process elements) and CEMP-r/s stars remains somewhat arbitrary and a robust identification framework is still missing[51]. In addition, both CEMP-s and CEMP-r/s stars seem to belong to binary systems[52] (and references therein), and the binary nature of the star cannot be used as a discriminant. The situation is currently not fully resolved; however, recent developments in physics-informed machine learning classification, using input features derived from nucleosynthesis models[53], offer promising avenues for improvement.

Recent developments aim to determine isotopic abundance ratios to identify the potential nucleosynthesis process behind the observed enrichment in heavy elements. Different isotopic mixtures are predicted for the *s*, *r* or *i* processes. Schematically, even-$N$ isotopes are mainly produced by the *s* process, while the contributions to the odd-$N$ isotopes coming from the *r* process is relatively higher. It remains difficult to estimate isotopic abundances by stellar spectroscopy, since the isotopic shifts (due to the different masses characterizing the isotopes of a given element) correspond to a few mÅ which is negligible when compared to the atomic line width. However, in contrast to even isotopes, the lines of the odd isotopes are additionally affected by hyperfine splitting, which in the case of Ba can reach some $\sim 50$ mÅ and can therefore be used to distinguish the nucleosynthetic process at its origin. In particular, this technique has been applied on the Ba line though with contradictory conclusions[54–57]. Recent high-resolution high-signal-to-noise observations have confirmed the technique on benchmarked stars[58] but also its sensitivity to three-dimensional (3D) as well as non-local thermodynamic equilibrium effects[59–61]. Such effects have also been shown to affect the determination of the elemental abundances deduced from observation, including those related to the Ba resonance line, potentially by as much as a factor of $\sim 5$. These observational uncertainties are currently limiting the interpretation of some observations, such as the open cluster observations mentioned above.

Substantial efforts in reducing the observational errors of abundance determinations from stellar photospheric atomic absorption lines are underway and are urgently needed to reduce systematic uncertainties. This involves the development and application of 3D hydrodynamical models of stellar atmospheres with non-local thermodynamic equilibrium radiation transport, and the use of high-resolution spectroscopy from large telescopes[60–62].

In order to advance the understanding of the *i* process and develop a solid observational data base to validate advanced astrophysics multi-scale, multi-physics simulations that integrate the new nuclear physics experimental, more of these exotic objects must be found. This is usually the first step, for example through large stellar surveys[63] such as GALAH[64] and APOGEE[65] and the upcoming 4MOST[66] and WEAVE[67] surveys, complemented with high-precision, high-resolution follow-up studies (e.g. Ref.[68]) with ground-based and space-based instruments in different wavelength regions. A selection of telescopes and instruments, used for abundance determinations, is provided as supplementary material.

## 3 The *i*-process engine

The observations described in the previous section point to a neutron source that operates at distinctly higher neutron densities than the *s* process but also distinctly lower than the *r* process. The so-called "convective-reactive" *i*-process engine provides the unique conditions to facilitate these intermediate neutron densities in the range $\approx 10^{13} - 10^{16}$ cm$^{-3}$. Reaching such high neutron densities poses a significant challenge, which is met by a two-step process. First, a neutron source species, in this case $^{13}$C, must be generated through the proton-capture (H-burning) reaction $^{12}$C(p,$\gamma$)$^{13}$N at low enough temperatures so that the $^{13}$N(p,$\gamma$)$^{14}$O reaction that would bypass $^{13}$C is avoided. This is typically the case at a temperature below $\approx 1.5 \times 10^8$K. Second, after the subsequent decay $^{13}$N$\to$$^{13}$C+$\beta^+ + \nu_e$), the neutrons must be released in the $\alpha$-capture (He-burning) reaction $^{13}$C($\alpha$,n)$^{16}$O that operates fast enough to produce sufficient neutrons only above a temperature of $\approx 2.7 \times 10^8$K[11–13]. Proton ingestion into a He-burning driven convection provides a convective-reactive interlocking of turbulent advection and nuclear transmutations[31]. The intricate balance of hydrodynamic and nuclear processes is the key to the *i*-process nucleosynthesis and is described in Box 1.

A major challenge is the potential termination of the process due to energy feedback from the $^{12}$C(p,$\gamma$)$^{13}$N reaction. While necessary for neutron production, this reaction can lead to a split in the convection zone in one-dimensional (1D) models[17,69]. When this takes place, the time and spatial average assumption of the mixing-length theory deployed to approximate convective transport in 1D stellar evolution is violated. Such a split of the convective zone has been studied in 1D models including a full coupling of diffusion and nucleosynthesis[69] and shown not to hinder the possible production of heavy elements by the *i*-process[70] while other studies find that a split prevents efficient *i*-process nucleosynthesis[17,31], reflecting that further work is needed. Nevertheless, the 3D macro physics of convection cannot be fully captured by 1D models on the basis of the mixing-length theory. 3D simulations demonstrate a more complex hydrodynamic feedback in the form of a non-radial Global Oscillation of Shell H-ingestion (GOSH)[71], capturing the 3D macro physics which in 1D simulations manifests as the convection zone split. The exact consequences of the 3D GOSH for the *i*-process nucleosynthesis, and if and how this process can be modeled in 1D simulations, are still under investigation. In either case, the feedback from energy release of the $^{12}C(p,\gamma)^{13}N$ reaction can lead to a termination of the *i*-process engine and implies an upper limit on the possible neutron density for *i*-process nucleosynthesis, with observable consequences that are still being established.

The *i* process can be simulated with escalating complexity, from simple one-zone network calculations with constant neutron density[19,46,72,73] or trajectory-based one-zone models[18], to multi-zone 1D stellar evolution models with inline[70,74,75] or post-processing nuclear reaction network simulations[31,76,77], and to 3D hydrodynamic simulations with nucleosynthesis post-processing using the advective two-stream method[20].

One-zone models and multi-zone 1D stellar evolution models are computationally efficient and can provide insights into the *i*-process nucleosynthesis, but they cannot fully capture the convective-reactive 3D macro physics of the *i*-process engine. These 3D macro-physics processes include, for example, rotation and magnetic fields, which are currently not included in 3D simulations of *i*-process sites and, as such, present simulations remain affected by modeling uncertainties. Improvements, as well as improving how 3D simulations are consistently connected to 1D progenitor stellar evolution models, are required in the future.

In view of the conditions needed for the *i*-process nucleosynthesis to take place, and simulations performed with different degrees of sophistication, various astrophysical sites have been explored. The most extensively studied models, both qualitatively and quantitatively, concern *i)* the AGB phase of metal-poor low-mass stars[16,17,70,74,75,78–83], *ii)* rapidly accreting white dwarfs[20,31,73,76,77] and *iii)* the very late thermal pulses of post-AGB stars[21,71]. These models have been relatively successful in explaining observations. Other possible astrophysical sites include the core helium flash of very low-metallicity low-mass stars[78,81,84–86], super-AGB stars ($7\ M_\odot \lesssim M \lesssim 10\ M_\odot$)[1] at low metallicity ($\lesssim 10^{-3}$)[87,88], and the helium shell of very low- or zero-metallicity massive stars ($M > 10\ M_\odot$) during central carbon burning or later stages[89–91]. Detailed nucleosynthesis models and a systematic comparison with observation is still missing for those scenarios.

**Box 1: The convective-reactive *i*-process engine**

[1] $M_\odot$ is the mass of the Sun

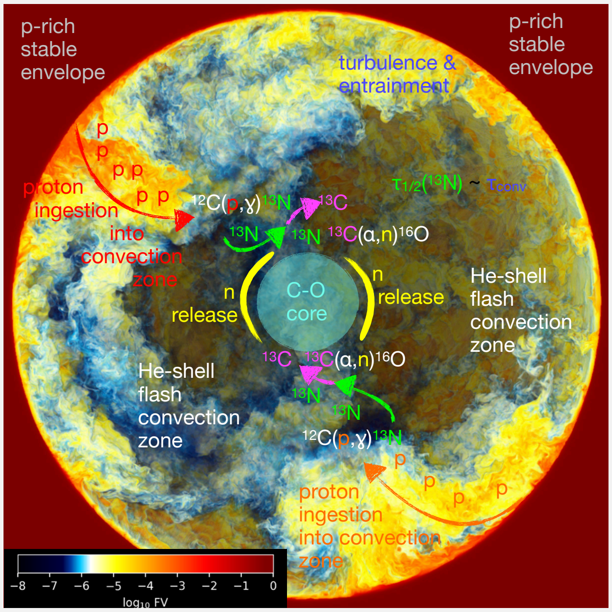


Schematic, of the *i*-process engine in a He-shell flash [20]. The background 3D image shows the concentration (fractional volume) of proton-rich material across the convection zone from the proton-rich envelope material (represented by the dark-red region) to the C-O core. The electron-degenerate C-O region, the pre-formed white dwarf, cannot be reached by protons as they are convective-reactively transformed to neutrons beforehand. Figure adapted with permission from Ref.[20].

The *i*-process engine is associated with a He-burning convection zone, here shown for the case of a He-shell flash in a rapidly accreting white dwarf simulation[20]. Protons from the H-rich envelope are entrained and advected through turbulent convection into the He-burning shell (shown along red and orange arrows) where the mass fraction of $^{12}$C is of the order 20 to 40%. From the outer region of the convection zone at the red-yellow transition toward the surface of the C-O core the temperature increases from $7 \times 10^7$ K to $2.7 \times 10^8$ K. When the inward-directed stream of protons reaches a temperature of $\approx 1.5 \times 10^8$ K the reaction $^{12}$C(p,$\gamma$)$^{13}$N is activated and may release a substantial and possibly flow-altering amounts of energy[71]. The newly formed $^{13}$N (olive-green region) with a half life of 9.6 minutes continues to be advected inward to even higher temperatures (green arrows). The radial convective transport takes place on the convective turnover time scale of approximately 15 minutes, incidentally similar to the nuclear $\beta$-decay time scale of $^{13}$N. Thanks to this, as soon as the decay happens in high-temperature conditions near the bottom of the He-shell flash convection zone, $^{13}$C emerges (purple arrows). At this point, the time scale for the $^{13}$C($\alpha$,n)$^{16}$O reaction is essentially instant, leading to a region (shown as yellow curves just outside the C-O core) of high neutron-density characteristic of the *i* process. It is the convective connection of the separate locations of the two reactions that give rise to the intermediate neutron densities of the *i*-process nucleosynthesis.

## 4 Nuclear physics of the *i* process

The astrophysics of the *i*-process engine (Section 3) allows for neutron densities up to $\approx 10^{16}\,\mathrm{cm}^{-3}$. In addition to the detailed modeling of the *i*-process engine, simulations need comprehensive reaction networks that include all relevant nuclear reactions and decay processes, providing the pathways through which elements are synthesized during the *i*-process nucleosynthesis.

The *i*-process pathway in the chart of the nuclides is driven by the competition between the $\beta^-$-decay and neutron-capture rates. Therefore, the most crucial nuclear-data inputs for modeling the *i* process are accurate neutron-capture and $\beta^-$-decay rates for a wide range of unstable, neutron-rich nuclei nuclei, particularly those approximately 1-10 neutrons away from the valley of stability (see Fig. 1).

For instance, the stable nucleus $^{56}$Fe (proton number $Z = 26$) serves as a seed nucleus in the *i*-process site. When exposed to the high flux of neutrons, successive neutron captures will take place on the stable iron isotopes $^{57}$Fe and $^{58}$Fe. Once the reaction path reaches an unstable isotope with a $\beta^-$-decay rate faster than the corresponding timescale against neutron capture, this isotope will undergo $\beta^-$ decay instead thus creating a new element Co, with proton number $Z = 27$. In this manner, the *i* process (similar to the *s* process) produces, through alternating neutron captures and $\beta^-$ decays, increasingly heavier elements until the neutron flux is exhausted, for example because of the termination of *i*-process engine (Sec. 3).

There are many hundreds of $(n,\gamma)$ reaction cross sections of unstable isotopes that are needed for a typical *i*-process reaction network calculation. The nuclear data needs are illustrated in the application of nuclear reaction networks [17,24,31,86,89], among others. For instance, the *i*-process network of Ref.[24] consists of 1160 individual nuclei extending to the superheavy element Cf. The network includes 2123 reactions in total, including neutron-, proton-, and $\alpha$-capture reactions in addition to $\alpha$ and $\beta^-$ decay and decay mediated by the electron-capture process. This network includes all species with $\beta^-$-decay half-lives greater than $\approx 1$ second, and can account for all reaction processes taking place in stellar environments at neutron densities up to $\approx 10^{17}$ neutrons/cm$^3$ at the *i*-process site. Measured nuclear data for both $\beta^-$-decay half-lives and neutron-capture reaction cross sections are typically available for near-stable and stable nuclei, respectively, from which the corresponding reaction rates can be deduced. However, for more neutron-rich unstable nuclei, less experimental information is available. In fact, out of the

1160 nuclei of relevance, 110 $\beta^-$-decay half-lives have not been measured and 793 (n,$\gamma$) reaction rates are not available from direct neutron-capture experiments (see e.g. Käppeler *et al.*, Ref.[5] for a review). This is because many of the unstable nuclei undergoing neutron capture in the *i* process are too short-lived, making it impossible to fabricate a sizable sample to expose to neutrons in the laboratory.

In addition to $\beta^-$-decay and neutron-capture rates, information on nuclear states, in particular their excitation energies as well as spin and parity quantum numbers, are of importance to account for possible thermalisation of these low-lying states in the nuclei present in the astrophysical environment. Quantum states with extraordinarily long lifetimes (isomeric states), could possibly play a role in the *i*-process nucleosynthesis. For example, isomers are plentiful in the neutron-rich Sr-Y-Zr region, as well as for neutron-rich In and Sn isotopes. While the impact of isomers on the *i*-process nucleosynthesis has not yet been investigated in detail, it may be possible that the presence of a non-thermalized isomer modifies the $\beta^-$-decay or neutron-capture timescales and consequently the reaction flow. In this case, isomers have to be treated separately from the ground state, as an individual species with all their corresponding nuclear properties.

When measured nuclear data for $\beta^-$-decay half lives and neutron-capture rates are not available, theoretical estimates are used. These have unknown systematic and parameter uncertainties that can impact nucleosynthesis predictions. With increasing neutron excess, deviations between model predictions tend to increase by factors of $\sim 10-20$ or even higher[92]. Experimentally, a factor of 2 or better (corresponding to a 95% confidence level) on neutron-capture rate uncertainties is targeted in measurements. Reductions in the uncertainties of the neutron-capture rates will significantly improve network calculations but the impact will be ultimately dictated by astrophysical modeling and observational uncertainties. In contrast, the experimentally missing $\beta^-$-decay half lives have been shown to have only limited influence[24].

Indirect experimental techniques (Section 6) with radioactive ion beams have been developed to constrain neutron-capture rates, however, such measurements are complex and time consuming. Impact and sensitivity studies are closely tied to specific astronomical manifestations of astrophysics processes, and significantly reduce the number of $(n,\gamma)$ reactions that need to be measured. Such studies assess the impact of nuclear physics uncertainties on simulation predictions of observables within a given astrophysical model. Reactions, impacting particularly valuable observations the most[21], can then be prioritized by experiments as they have the highest potential to constrain the physics of the *i* process, including the 3D macro physics of the *i*-process engine. Recent studies have identified the most relevant reactions for several of the most important observations[21,46,73,92] described in Section 2. Experimentally determined neutron-capture cross sections serve as important constraints to models as will be discussed next.

## 5 Theoretical neutron-capture reaction rates

Calculations of the neutron-capture cross section are classically based on the statistical Hauser-Feshbach model[93]. Such a model makes the fundamental assumption that the capture process takes place with the intermediary formation of a compound nucleus (CN). The energy of the incident particle is then shared more or less uniformly by all the nucleons before releasing the energy by particle emission or $\gamma$-ray decay. The neutron-capture cross section $\sigma_{n,\gamma}(E_n)$ at an incident neutron energy $E_n$ is expressed as the conditional probability to form the CN and to decay by $\gamma$-ray emission, i.e. in a simplified form

$$\sigma_{n,\gamma}(E_n) \propto \sum \frac{T_n T_\gamma}{T_n + T_\gamma} \sim \sum T_\gamma \tag{1}$$

where the summation runs over all the CN excited states, $T_n$ is the neutron transmission coefficient and

$$T_\gamma = \sum_{J^\pi, XL} \int_0^{S_n+E_n} 2\pi E_\gamma^{2L+1} f_{XL}(E_\gamma) \rho(E_x - E_\gamma, J, \pi) dE_\gamma \tag{2}$$

is the total $\gamma$-ray transmission coefficient obtained by the folding integral, over all $\gamma$-ray energies ($E_\gamma$) and intermediate states of energy $E_x$ up to $E_x = S_n + E_n$, spin $J$ and parity $\pi$, of the nuclear level density (NLD) $\rho(E_x - E_\gamma, J, \pi)$ and the $\gamma$-ray strength function ($\gamma$SF) $f_{XL}(E_\gamma)$. Further, $S_n$ is the neutron separation energy, i.e. the minimum energy required to remove a neutron from the CN. The NLD and $\gamma$SF describe the average nuclear properties in the region of high-excitation energies known as the quasi-continuum. The NLD represents the number of excited quantum states per energy interval, and the $\gamma$SF reveals the distribution of the electromagnetic decay strength[94]. The $\gamma$SF is characterized by the electromagnetic mode $XL$, where $X$ is either electric or magnetic radiation and $L$ is the angular momentum carried by the $\gamma$ ray. The electromagnetic transitions of the $\gamma$SF obey the quantum-mechanical selection rules determined by the spins and parities of the initial and final levels. Since the strong nuclear interaction gives rise to a neutron transmission coefficient much larger than the electromagnetic one, i.e. $T_n \gg T_\gamma$, at the tens of keV energies of interest for nucleosynthesis applications, the neutron-capture cross section essentially depends on $T_\gamma$, i.e. on the NLD and $\gamma$SF of the CN. The statistical model is able to predict cross sections typically within 50% for the particular case of neutron captures. For nuclei of relevance to the *i*-process nucleosynthesis, the estimate of $\sigma_{n,\gamma}(E_n)$

suffers from uncertainties stemming essentially from the predicted NLDs and γSFs[95], discussed here below, as the nuclear masses are known experimentally.

### 5.1 NLD models

NLDs have been the subject of many studies[96] since the pioneering work of Bethe[97], who provided the first analytical expression for the number of excited levels in a heavy nucleus at a given excitation energy $E_x$. This Fermi gas formula has been improved along the years to take nuclear shell, pairing, deformation and collective effects into account[98,99]. The most popular analytical expressions are the back-shifted Fermi gas or the constant-temperature models. Going beyond parametrized analytical formulae, NLD models based on more microscopic approaches describing the effective interaction and excitation of nucleons have been developed. These include the independent-particle statistical model[100] and the combinatorial approach[101–103]. Another category of models relies on the configuration interaction approach and employs matrix diagonalisation within a truncated orbital space[104]. This approach encompasses the nuclear shell model and its various adaptations and include correlations beyond mean-field theory. However, their applications, even within the promising Monte Carlo[105] or projected[106] shell models for the time being can hardly be extended to the hundreds of nuclei relevant to *i*-process nucleosynthesis. The recent quasi-particle random phase approximation (QRPA) plus boson expansion method[107] also moves beyond the independent-particle approximation and exhibits promising predictive power in incorporating low-energy correlations.

### 5.2 γSF models

High-energy γ-ray decay has been characterized by a Lorentzian shape, which describes the giant dipole resonance (GDR), a collective nuclear excitation mode where protons and neutrons in a nucleus oscillate against each other. Over the years, this Lorentzian model has been refined to include an energy-dependent width, as predicted by the Fermi liquid theory[108]. Given the significant impact of GDR properties and low-energy resonances on capture cross-section predictions, microscopic γSF models have been developed for improved reliability and predictive power. Since the early 1970s, various mean-field approaches, such as the QRPA, the quasiparticle-phonon model, and their improved variants, have been applied to describe giant multipole resonances in both non-relativistic and relativistic frameworks. The nuclear shell model has also been extensively used to describe electromagnetic excitations, though mainly for light nuclei with the exception of the Monte Carlo and projected shell models which have been applied to heavy nuclei as well[109,110]. Despite advancements in microscopic models, only a few attempts have been made to provide systematic large-scale calculations of both the electric ($E1$) and magnetic ($M1$) dipole modes that can compete with more phenomenological Lorentz-type models. γSFs obtained within the non-relativistic Hartree-Fock Bogoliubov (HFB) plus QRPA framework have shown satisfactory agreement of the GDR location and width, as well as a wide range of other γSF-related observables[111]. Similar attempts within the relativistic mean-field framework have been made in a less systematic manner[112,113].

When examining the de-excitation γSF, deviations from the photo-absorption strength are expected, especially as γ-ray energies approach zero. Experimental evidence has confirmed a low-energy enhancement in the de-excitation γSF[114,115] of dipole[116,117]and possibly magnetic character[117]. Self-consistent, temperature-dependent QRPA calculations have been proposed to explain this low-energy upbend, suggesting it has an $E1$ character[118]. Nuclear shell model and projected shell model calculations indicate a possible $M1$ origin for this phenomenon instead[110,119]. Interestingly, shell models results also suggest a link between the upbend and the scissors mode where protons and neutrons oscillate against each other like the blades of a pair of scissors[110,120,121]. The discovery of the low-energy enhancement has spurred new theoretical and experimental research into low-lying $M1$ strength as well as detailed analyses of its potentially large impact on reaction rates[122] and the *i*-process nucleosynthesis[24].

### 5.3 Uncertainties of (n,γ) capture rates

Both the NLD and γSF predictions are affected by nuclear model (or equivalently "systematic") and nuclear parameter (often referred to as "statistical") uncertainties that influence the prediction of the neutron-capture rates. While the systematic uncertainties are correlated by the underlying model, the uncertainties associated with local variations of the model parameters are uncorrelated. Both uncertainties need to be constrained by experimentally known observables. These include the level spacing at $S_n$ for NLD[96] and average decay probabilities (total radiative widths) of these resonances or photoabsorption data for γSF[111], and measured cross sections.

One example on the interplay of impact studies, model uncertainties and associated experimental constraints is the $^{139}$Ba$(n,\gamma)^{140}$Ba reaction. It has been identified to be crucial for using the observed Ba/La ratio to distinguish *i*-process from *s*- and *r*-process stars[73]. A measurement that significantly constrains the model uncertainties is shown in Fig. 3. The measurement is instrumental to reduce nuclear data uncertainties sufficiently so that its impact on model predictions is smaller than the astronomical observational uncertainty, thus validating an *i* process neutron density of $\approx 10^{13}$ cm$^{-3}$ in CEMP stars. It is vital to collect additional targeted experimental data on neutron-capture rates with indirect measurements to constrain the underlying quantities that enter the neutron-capture rate calculations to reduce their at-present very large uncertainties.

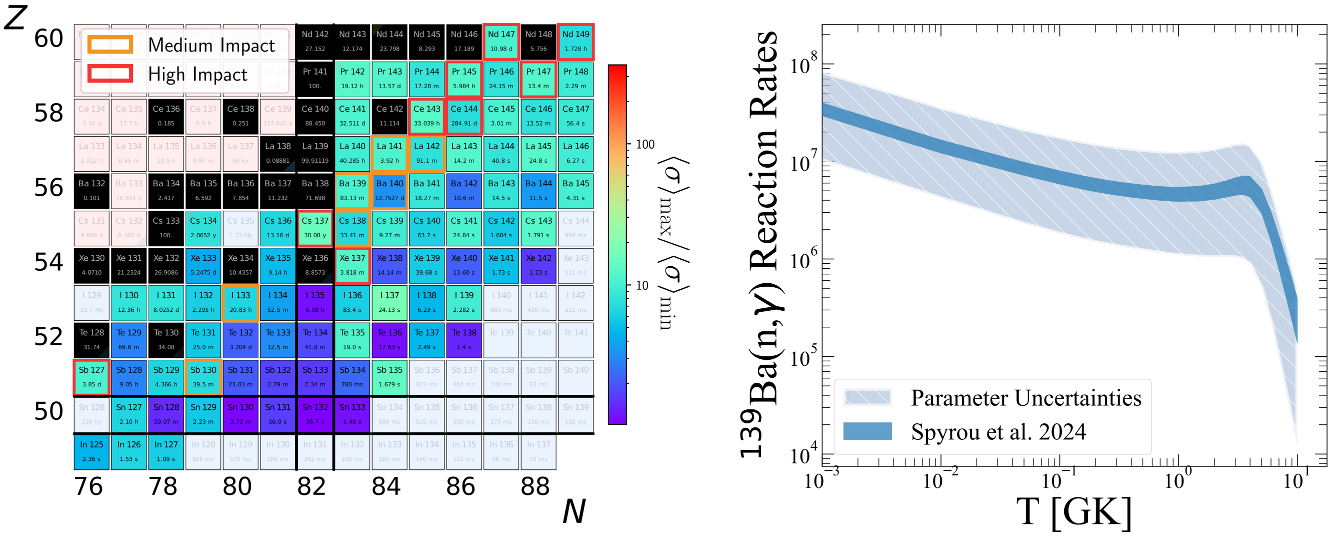


**(a)** **(b)**

**Figure 3. Impact of Reaction Rate Uncertainties on the *i* Process**
Panel (a): Chart of the nuclides in the Sn–Nd region highlighting the nuclei and neutron-capture reactions relevant to the *i*-process nucleosynthesis in low-mass, low-metallicity AGB stars. The reactions on these nuclei are color-coded by their uncorrelated parameter uncertainty (the ratio between maximum and minimum rates). In addition, systematic model uncertainties would have to be taken into account. Some of the reaction targets for which the parameter uncertainties have a medium or high impact on one or multiple isotopic *i*-process abundances are emphasized by an orange or red square contour, respectively[92]. Panel (b): One of the highest-impact reactions[73], $^{139}$Ba(n,$\gamma$)$^{140}$Ba, is affected by parameter uncertainties reaching a factor of about 10 between the maximum and minimum rates. It has recently been experimentally constrained by Spyrou *et al.*[43]. The corresponding 85% reduction in the uncertainties for this rate leads to a decrease by a factor of 4 of the total uncertainty in the La production by the *i* process[92]. Figure panel (b) adapted with permission from Ref.[92].

## 6 Experimental techniques

While it would be ideal to directly measure (n,$\gamma$) reaction rates for the *i* process, such measurements are out of reach for now due to the lack of a suitable targets of neutrons or short-lived isotopes. Therefore, experimental programs focus on constraining neutron-capture reaction rates through indirect techniques.

In most studies, two key experimental observables are the NLD and $\gamma$SF. The most commonly used experimental techniques, described here, focus on constraining (n,$\gamma$) reaction rates indirectly for unstable nuclei through measurements, following reactions with charged-particle beams. These measure the product of the NLD and $\gamma$SF (6.1, 6.2) or the $\gamma$SF (6.3, 6.4) and NLD (6.5) separately, see Box 2 for details on measuring these observables. State-of-the-art research infrastructure is a critical component for successful measurements and is discussed in more detail as supplementary material.

**Box 2: Measuring $\gamma$SF and NLD**

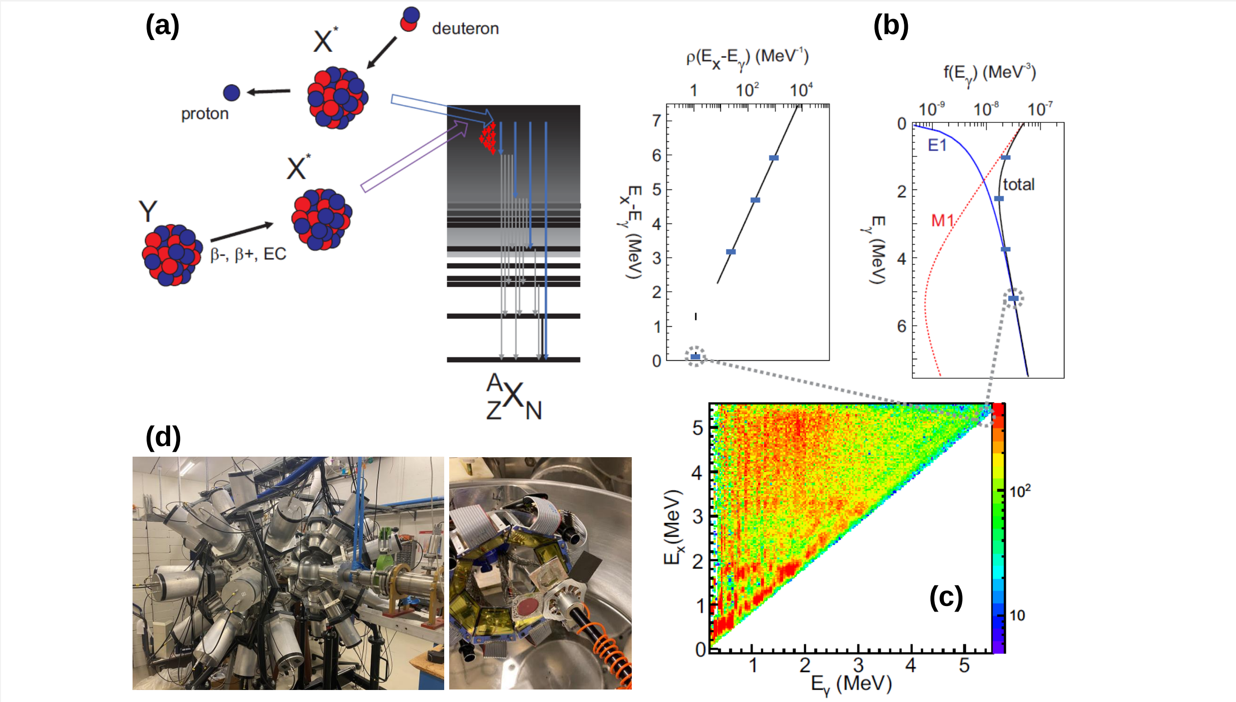


The first step of all indirect techniques for constraining the (n,$\gamma$) cross section described in this review is the population of states in an excitation energy regime with high NLD in a nucleus through either a charged-particle reaction or $\beta^-$ decay that leads to an excited nucleus $X^*$ as depicted in (a). A distribution of highly-excited states with a range of excitation energies, spins and parities is being populated according to the population mechanism. When the NLD exceeds approximately 10 levels per MeV, these states can be considered to exhibit statistical $\gamma$-ray decay behaviour and can therefore be described by the $\gamma$SF. The different characteristics of the states populated in either charged-particle reactions or $\beta^-$ decays compared to the population in direct neutron-capture reactions need to be taken into account. A schematic NLD and $\gamma$SF are shown in (b) with the $\gamma$-ray transitions $E_\gamma$ being primarily of dipole character. At high $E_\gamma$ the $\gamma$SF is dominated by $E1$ transitions. At low $E_\gamma$ energies, a low-energy enhancement is sometimes observed. Whether this upbend is of $E1$ or $M1$ character remains to be experimentally determined, although most theoretical calculations predict $M1$ radiation[110,120,121]. For the $\gamma$-ray transitions displayed in (a) there are corresponding lines in (b) where $E1$ (blue line) and $M1$ (red line) contributions are indicated. The distribution of primary $\gamma$ rays (i.e., the first $\gamma$ ray emitted in a $\gamma$-ray cascade) as a function of excitation energy $E_x$ in (a) is presented as a matrix (c) used in the Oslo method analyses. The relative intensity of the individual $\gamma$ rays, $E_\gamma$, depopulating a specific state at an excitation energy, $E_x$, is proportional to the product of the $\gamma$SF at $E_\gamma$ and the NLD at the final states with an energy of $E_x - E_\gamma$, according to Eq. (4). An example is shown for the highest-energy $\gamma$-ray transition with $E_x = E_\gamma$ (largest purple transitions), and its location is indicated by circles in (b) and (c). The surrogate reaction method measures the behavior of $\gamma$-ray transitions from lower excitation energies instead (gray transition in (a)). In (d) a typical experimental setup is shown with the Oslo Scintillator Array[123] (left) and the ring of silicon detectors[124] (right) to detect in coincidence $\gamma$ radiation and light-charged particles, respectively.

### 6.1 Surrogate Methods

The Surrogate Reaction Method (SRM) uses an alternative reaction to neutron capture to populate the nucleus of interest and derive constraints for the determination of (n,$\gamma$) cross sections via the interplay and advances in theory and experiment[125–131]. The SRM uses Hauser-Feshbach reaction theory to calculate reaction cross sections described by the formation of the CN and the decay into the $\gamma$-ray channel for the case of (n,$\gamma$) reactions. Theoretical developments in the SRM led to a formalism describing the coincidence probability between charged particles and emitted $\gamma$-rays in the exit channel. The coincidence probability $P_{\delta\chi}(E_x)$, with a cross section for forming the CN, $F_\delta^{CN}(E_x,J,\pi)$[128], and the decay of the CN via $\gamma$-ray emission,

$G_\chi^{CN}(E_x,J,\pi)$[130], is expressed as:

$$P_{\delta\chi}(E_x) \quad = \quad \sum_{J,\pi} F_\delta^{CN}(E_x,J,\pi)\ G_\chi^{CN}(E_x,J,\pi)\,, \tag{3}$$

where $\delta$ refers to the formation of the CN in the surrogate reaction and $\chi$ to the decay channel of interest. The product of the $\gamma$SF and the NLD is contained in the factor $G_\chi^{CN}(E_x,J,\pi)$, but the two quantities are usually not extracted explicitly. A theoretical framework to extract the NLD and $\gamma$SF from the SRM has recently been developed[132].

SRM experiments require high-resolution $\gamma$-ray spectroscopy coupled with highly-segmented charged particle-arrays (e.g for proton detection). Characteristic $\gamma$-rays toward the bottom of the $\gamma$-ray cascade that de-excite the initial entry state in the CN are detected in coincidence with outgoing charged particles to obtain their coincidence probability. By comparing the calculated and measured coincidence probabilities, $P_{\delta\chi}(E_x)$, it is possible to constrain the parameters that describe the decay of the CN, which ultimately leads to (n,$\gamma$) cross section constraints.

Implementations of the SRM in inverse kinematic reactions has recently begun at various facilities allowing access to *i*-process nuclei as long as accelerated particle beam intensities are sufficiently high ($10^6$ per second or higher).

The Surrogate Ratio Method is a variation of the SRM in which two surrogate reactions are utilized to obtain a relative $\gamma$-decay probability ratio[133–137]. The reaction of interest is measured relative to a reference reaction from the same isotopic chain. Implementations relevant to the *i*-process are currently being explored.

### 6.2 The Oslo method

NLDs and $\gamma$SFs for *i* process nuclei can be inferred using the Oslo method. The foundation for the method was laid more than forty years ago[138] and has continuously been developed and improved[139–141]. The strength of the method is that no assumptions need to be made on the functional form of the NLD or the $\gamma$SF, and that both functions can be extracted from the very same data set. These functions need to be normalized[142] and the standard procedure is based on three normalization points: (i) the density of discrete levels, (ii) the density of levels from the average neutron resonance spacings at the neutron separation energy, and (iii) the average total radiative width. However, for *i*-process nuclei, these latter two anchor points may not be available due to experimental difficulties to obtain these quantities for unstable nuclei. Very often, reasonable estimates have to be made based on empirical systematics and/or theoretical predictions.

The Oslo method relies on measuring $\gamma$-ray spectra as a function of excitation energy $E_x$. The spectra are unfolded with the $\gamma$-detector response functions[143], and the primary $\gamma$ spectra are extracted through an iterative procedure[144]. The primary spectra are stored in a matrix denoted by $P(E_\gamma,E_x)$ (see Box 2 for an example). Since the $\gamma$SF depends only on the $\gamma$ energy, $E_\gamma$, according to the generalized Brink-Axel hypothesis[145,146], one can factorize, applying Fermi's golden rule,

$$P(E_\gamma,E_x) \propto \rho(E_x-E_\gamma)\cdot\mathscr{T}(E_\gamma), \tag{4}$$

and extract the level density $\rho(E_x-E_\gamma)$ and partial $\gamma$-ray transmission coefficient $\mathscr{T}(E_\gamma)$. In comparison to the total $\gamma$-ray transmission coefficient, $T_\gamma$, (see Sec. 4), the connection between the partial transmission coefficient and the $\gamma$SF is $f_{XL}(E_\gamma)=\mathscr{T}(E_\gamma)/(2\pi E_\gamma^{2L+1})$ for specific $\gamma$-ray transitions with angular momentum $L$. There exist various complementary Oslo-type techniques to obtain the key $P(E_\gamma,E_x)$ matrix.

In the *Standard-Oslo method* stable light-ion beams on stable or long-lived targets are used. By requiring only one outgoing charged particle (ejectile), the energy of the ejectile determines the initial excitation energy of the residual nucleus. A typical reaction that can provide information on the *i* process is the $(\alpha,p\gamma)$ reaction[147] on the most neutron-rich stable or long-lived targets. The charge-exchange reaction mechanism, where one nucleon type in the beam-target combination is exchanged for another, has also been used in conjunction with the Oslo method. The Standard-Oslo method allows for some but not the majority of *i*-process nuclei to be studied as they lie beyond the reach of stable beam and target reactions.

The *Inverse-Oslo method* is based on inverse reactions where the heavy nucleus is now the beam, while the light particle is the target. The first application of the Inverse-Oslo method used accelerated stable $^{86}$Kr and the d($^{86}$Kr,p$\gamma$)$^{87}$Kr reaction as a proof-of-principle that the Oslo method could indeed be applied in inverse-kinematics experiments[148]. The use of radioactive beams opens up a wide range of neutron-rich nuclei relevant to the *i* process that can be studied. The first measurement with radioactive beams was the d($^{66}$Ni,p$\gamma$)$^{67}$Ni reaction, which studied the sensitivity of the $^{66}$Ni$(n,\gamma)^{67}$Ni neutron-capture reaction on *i*-process nucleosynthesis[149]. The limiting factor is the beam intensity requirements which are similar to that of the SRM, in addition to the degraded excitation-energy resolution compared to what can usually be achieved in normal kinematics.

In the $\beta$*-Oslo method* excited states in the nucleus of interest are populated following $\beta^-$ decay[150–152]. The advantage of $\beta^-$ decay is that it can be used with very low beam intensities, of roughly one particle per second and nuclei much farther from the valley of stability can be accessed, which are out of reach for other techniques. The $\beta^-$ particles do not carry excitation energy information and the $\beta$-Oslo method requires the use of segmented total absorption $\gamma$-ray spectrometers (TAS). The full $\gamma$-ray energy deposited into the TAS corresponds to the populated excitation energy, while the segmentation enables the extraction of the individual $\gamma$-ray energies. With this information, the $P(E_\gamma, E_x)$ matrix can be constructed and the rest of the analysis follows the Standard-Oslo method. The limitation is the requirement of populating excitation energies sufficiently high, determined by the reaction energetics of $\beta^-$-decay. In recent years, the open questions in *i*-process nucleosynthesis have motivated several $\beta$-Oslo experiments, most of which are still under analysis. One of the first of these investigations studied the *i* process relevant $^{139}$Ba(n,$\gamma$)$^{140}$Ba reaction[43] shown in Fig. 3.

### 6.3 The Shape method

While the Oslo method is a widely used technique to extract the $\gamma$SF and NLD it relies on external normalization factors that are typically unavailable for unstable nuclei. To address this limitation, the Shape method[153] offers a complementary approach by analyzing $\gamma$-ray decays from the quasi-continuum into discrete low-lying states. For a given range of excitation energies, the intensity ratio of $\gamma$-ray decays into specific low-lying states directly reflects the ratio of the $\gamma$SF values at the corresponding $\gamma$-ray transition energies. The Shape method employs this relationship in an iterative procedure to determine the functional form, or "shape", of the $\gamma$SF. This enables an absolute determination of the slope parameter of the $\gamma$SF in the Oslo method analysis, though the absolute magnitude of the $\gamma$SF is still unconstrained by data.

In combination with the Oslo method, the Shape method also allows extracting the "partial" absolute NLD of those states populated in an experiment. The Shape method has successfully reproduced known $\gamma$SF and NLD results from stable-target and $\beta$-Oslo experiments, populating unstable nuclei[154]. The method was also used to refine the $\gamma$SF and NLD of $^{140}$Ba and $^{93}$Sr, leading, respectively, to revised estimates for the $^{139}$Ba(n,$\gamma$)$^{140}$Ba[43] and $^{92}$Sr(n,$\gamma$)$^{93}$Sr[155] cross sections.

### 6.4 Coulomb excitation and dissociation

Relativistic Coulomb excitation and dissociation (CED) has been applied to measure the $\gamma$SF in exotic nuclei. In this method, rare isotopes are produced and the fast projectiles are impinged on high-$Z$ targets. Within the target the projectile experiences a time-varying electromagnetic field, which can induce excitation. The de-excitation takes place through $\gamma$ rays (below the neutron separation energy) or neutrons (above the neutron separation energy), and is measured as a function of excitation energy. The Coulomb dissociation cross section of the mass $A$ projectile for ($\gamma$,n) is extracted and the $(n,\gamma)$ cross section to the ground state of the projectile from the $A$-1 mass nucleus can be constrained through the detailed balance principle[156]. CED can provide much needed information on the $\gamma$SF above the neutron separation energy in stable and neutron-rich nuclei[157–162]. Additional measurements would be highly beneficial to explore the variation of the $\gamma$SF across the chart of the nuclides and to provide constraints to the absolute normalizations of indirect techniques such as the Oslo methods.

### 6.5 Particle-Evaporation technique

The particle-evaporation technique enables constraints of the NLD integrated over the populated spins and parities[163] from measurements of double differential cross sections, which is the probability of a nuclear reaction occurring while measuring two independent variables, such as energy and angle, of outgoing particles from reactions leading to a CN. The method has been successfully applied to stable nuclei (Refs.[164–166]). Future implementations of this technique using $^{6,7}$Li or $^{12}$C-induced reactions, as well as ($\alpha$,p) or similar reaction channels with stable beams and extension of the method to inverse kinematic reactions, will enable this technique to be applied to *i*-process nuclei.

These indirect experimental techniques enable the determination of (n,$\gamma$) reaction rates via the Hauser–Feshbach model that can then be incorporated into simulations of *i*-process nucleosynthesis.

## 7 *i*-process simulations

To illustrate state-of-the-art simulations of the *i*-process nucleosynthesis taking place in astrophysical sites, we consider the two most extensively studied sites (i) the proton ingestion during the thermal pulse He-shell flash in very low-metallicity low-mass AGB stars; (ii) the rapid accretion of H-rich material on white dwarfs. Both models can reproduce the heavy element patterns in CEMP-r/s stars [20,31,70,75,77]. Fig. 4 illustrates the abundance distributions resulting from both models and compares them with those observed in the CEMP-r/s star CS31062-050 of metallicity $[\mathrm{Fe/H}] = -2.5 \pm 0.15$. This star would have been polluted by *i*-process-enriched material transferred from its binary companion.

Despite the recent success of nucleosynthesis studies, the details of *i*-process simulations are still affected by a variety of uncertainties, including in particular those associated with the astrophysical modeling, described in Sec. 3, and the determination of neutron-capture reaction rates of the neutron-rich nuclei involved, as discussed in Secs. 4, 5 and 6. Nuclear uncertainties essentially stem from unknown $\gamma$SFs and NLDs. As mentioned previously, both model and parameter uncertainties impact the predictions of these quantities, and need to be considered before being propagated into reaction rates and astrophysical simulations.

Both the correlated model and uncorrelated parameter uncertainties have been coherently estimated before being propagated to astrophysical observables through multi-zone stellar evolution models[92], as illustrated in Fig. 4 for one specific AGB

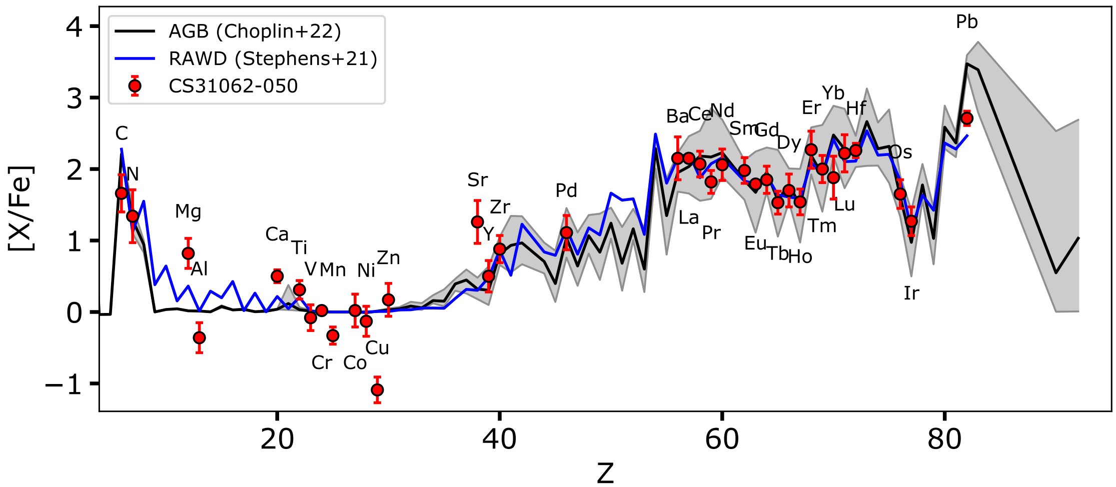


**Figure 4. Observed and Modeled Abundance Distributions**
Comparison of the elemental abundance distributions in terms of the astronomical notation [X/Fe], which is the logarithm of the abundance ratio of element X to Fe relative to the same ratio in the Sun, of the CEMP-r/s star CS31062-050[26,167–169]. Shown are also the model predictions for an *i* process in a $M = 1M_{\odot}$, [Fe/H]=-2.5 AGB star (black line)[74] as well as a 3D stellar-hydrodymamics simulation based on predictions with the advective two-stream post-processing method for a rapidly accreting white dwarf (RAWD, blue line)[20]. The AGB abundance distributions include the propagation of nuclear parameter uncertainties (grey shaded area)[92]. Observed abundances are compiled for the different elements from various works[26,167–169] and were not all derived using the same model atmosphere parameters and assumptions. Outliers, such as Sr, are interesting and highlight the need for future work. Observational error bars include statistical but not systematic uncertainties.

model. Many reactions are found to affect the nucleosynthesis predictions and will require improved nuclear models guided by experimental constraints. Priority should be given to the reactions influencing the observable tracers (Sec. 2), as detailed in Refs.[73,92].

Additionally, it has been shown that, while the main *i*-process path ends in a Pb-Bi-Po cycle, a potentially non-negligible fraction of the nuclear flow can bypass the rapidly $\alpha$-decaying Po-Ac region and reach the actinide region, as detailed in Box 3. Although it has been widely believed that actinides, and most particularly Th and U, are exclusively produced by the explosive *r*-process nucleosynthesis[6,7], actinides are found to be potentially synthesized through the *i*-process nucleosynthesis, provided neutron densities of $N_n \gtrsim 10^{15}\text{cm}^{-3}$ are achieved in the astrophysical site. Such conditions can be found in 1D low-mass low-metallicity AGB models[74], but Th and U enrichment remains strongly affected by nuclear data uncertainties along the production path (see Fig. 4), especially in view of the uncertain $^{217}$Bi(n,$\gamma$)$^{218}$Bi reaction rate[92], but also by astrophysical modeling of the *i*-process site, including the GOSH instability described in Section 3.

Observational confirmation of the presence of Th at the surface of CEMP stars remains spectroscopically challenging. One stellar candidate that may confirm the production of actinides by the *i* process is the CEMP r/s-star RAVE J094921.8-161722[170] that shows Th absorption lines in its spectrum. Future observations may confirm this possibility for the *i* process to produce actinides and open the way to cosmochronometry which would provide a lower limit on the age of the CEMP-r/s star, provided surface abundances of both Th and U can be extracted simultaneously[74].

As illustrated in Fig. 4 and detailed in Sec. 3 present *i*-process simulations have proven their capacity to explain observations that could not be described by other processes. However, they remain affected by uncertainties associated with astrophysics modeling and nuclear physics predictions, both of them having a potential impact on nucleosynthesis predictions.

**Box 3: The Endpoint of the *i* Process**

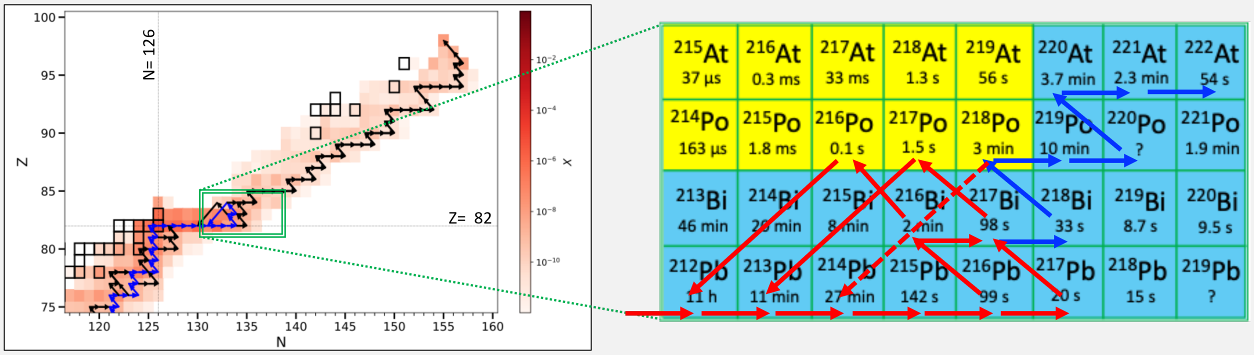


The termination point of the *i* process is currently an open question. The reaction flow can continue to heavy masses through consecutive neutron capture and $\beta$ decays, depending on the astrophysical conditions and on the nuclear reaction rates. In some scenarios, like in low-metallicity low-mass AGB stars, the neutron density reaches values above $\approx 10^{15}\text{cm}^{-3}$, so that the *i* process is found to even contribute to Th and U production[74, 171], which so far has been attributed exclusively to the *r* process. The possibility of extending into the actinide region is defined by an important branching point which appears at $^{217}$Bi. Here, due to the large uncertainty in the $^{217}$Bi(n,$\gamma$)$^{218}$Bi reaction cross section, the competition between neutron capture and $\beta$ decay is not obvious. Two possibilities exist depending on the rate of the $^{217}$Bi(n,$\gamma$)$^{218}$Bi reaction, as shown in the left figure with an AGB star calculation showing the *i*-process reaction network starting at $Z = 75$[74]. The right figure shows a zoomed-in version of the Pb-Bi-Po-At region to highlight the half-lives and dominant production and decay paths. Isotopes in yellow decay predominantly via $\alpha$ decay, while the ones in blue decay via $\beta$ decay. Red and blue arrows show the two competing paths branching at $^{217}$Bi detailed below, while the red-dashed line shows the $\alpha$ decay of $^{218}$Po which is not favored here. There are two possible scenarios:

1. Termination at the Pb-Bi-Po cycle (red arrows, right side of figure)
   If the $^{217}$Bi $\beta$ decay dominates, then the flow reaches $^{217}$Po, an $\alpha$ emitter with a short half-life (1.5 seconds). The $\alpha$ decay of $^{217}$Po brings the flow back to $^{213}$Pb, terminating the *i* process in the Pb-Bi-Po cycle.

2. Termination beyond actinide nuclei (blue arrows, right side of figure)
   If the $^{217}$Bi(n,$\gamma$)$^{218}$Bi reaction wins over $\beta$ decay, the flow changes drastically. This is because $^{218}$Bi $\beta$ decays into $^{218}$Po, which has a 3 minute half-life, long enough for neutron-capture reactions to dominate over $\alpha$ decay. This allows the flow to continue to heavier elements and contribute to actinide production. In this scenario, the termination is not clear since the reaction network[74] was artificially terminated at $^{253}$Cf (left figure).

Understanding the *i*-process endpoint has significant consequences in our understanding and interpretation of stellar observations. The observation of Th and U in metal-poor stars has been interpreted to originate from *r*-process events. This cannot be guaranteed however, if the *i* process has significant actinide production. Recent work[171] also shows that the production of actinides can provide detectable signatures in future $\gamma$-ray observations of $^{208}$Tl. Left side of figure adapted with permission from Ref.[74].

## 8 Concluding remarks

Understanding the origin of the chemical elements remains one of the fundamental questions in physics. The classical nucleosynthesis picture has long been dominated by stellar burning processes, and the well-established *s*, *r*, and *p* processes. New discoveries in observational astronomy, nuclear astrophysics, and experimental and theoretical nuclear physics have made the *i* process to become increasingly recognized as an important piece to the puzzle. Observational evidence from CEMP-r/s and AGB stars support the existence of neutron-capture nucleosynthesis operating at intermediate neutron densities between those for the *s* and *r* processes. However, to integrate the *i* process into our overall understanding of how the elements form, several fundamental challenges must still be addressed.

A key outstanding question is: What are the precise stellar conditions in which the *i* process occurs across different astrophysical sites? A range of environments are suggested - such as proton ingestion episodes in low-metallicity AGB stars, very late thermal pulses in post-AGB stars, and rapidly accreting white dwarfs - but the associated neutron densities, ranging from $\sim 10^{13}$ to $10^{16}$ cm$^{-3}$, remain impacted by many modeling uncertainties. This difficulty directly affects model predictions for key elemental abundance ratios such as [Ba/La], [Sr/Ba], and [Eu/La], which are used as diagnostics of the *i* process.

Tightly constraining the neutron densities in *i*-process sites is of utmost importance. A promising approach involves using abundance ratios that are very sensitive to the neutron-capture path and depend on nuclear reaction flows near closed neutron shells. While some indirect measurements, such as those constraining the $^{139}$Ba(n,$\gamma$)$^{140}$Ba reaction, have significantly reduced nuclear reaction uncertainties, many relevant (n,$\gamma$) reaction rates for short-lived nuclei remain experimentally unconstrained. As an example, the [Sr/Y/Zr] ratios are influenced by $(n,\gamma)$ cross sections near the $N = 50$ shell closure with many isotopes directly involved in shaping the first *i*-process abundance peak and offer insight into predicted neutron fluxes.

A practical solution to having a majority of unconstrained (n,$\gamma$) reaction rates lies in prioritizing high-impact reactions identified via sensitivity and impact studies, followed by experimental campaigns using indirect techniques like the $\beta$-Oslo method, Inverse-Oslo method and the Surrogate Reaction Method enabling access to neutron-rich isotopes previously beyond reach.

On the observational side, abundance determinations still suffer from significant systematic uncertainties. Promising solutions include the development of full 3D stellar atmosphere models to improve abundance extractions, particularly for key elements like Ba, La, and Eu. Also, high-resolution, high signal-to-noise spectroscopy from large telescopes targeting a statistically significant sample of CEMP-r/s stars from observational surveys are required to provide more precise observational constraints.

From a theoretical perspective, there is a pressing need to reduce uncertainties in 3D hydrodynamical models of *i*-process sites. In particular, models need to better capture the feedback between nuclear energy generation and convective dynamics, especially in the presence of instabilities like the GOSH. Current 3D simulations are limited by computational timescales and lack of rotation or magnetic field effects. Proposed improvements include the systematic coupling of 3D hydrodynamics with nucleosynthesis post-processing, ideally connected back to full stellar evolution models and the implementation of rotational and magneto-hydrodynamic effects,

The potential for *i*-process actinide production (e.g., Th, U) represents a transformative opportunity and if confirmed would necessitate a reevaluation of current assumptions about the origin of actinides, which has been attributed exclusively to the *r* process. However, theoretical predictions hinge on the uncertain $^{217}\mathrm{Bi}(n,\gamma)^{218}$Bi reaction rate, among others, and observational confirmation remains tentative.

Moving forward, a multidisciplinary concerted effort between astronomers, nuclear physicists, and theoretical astrophysicists will be essential for a full understanding of the *i* process. Through collaborative frameworks and networks, the research community is able to integrate observational data, astrophysical simulations, targeted nuclear physics measurements, theories and models. In doing so, it is possible not only to address outstanding questions in nucleosynthesis but also to deepen the understanding of stellar evolution and the cosmic chemical landscape.

## Glossary terms

- *s* process: The slow neutron-capture process is one of the nucleosynthesis pathways by which elements heavier than iron are formed in stars. It occurs in stellar interiors under conditions where neutron capture proceeds slowly relative to $\beta$ decay.
- *r* process: The rapid neutron-capture process is a nucleosynthesis process producing elements heavier than iron where the neutron capture proceeds fast with respect to $\beta$ decay. It involves an extremely high neutron flux.
- *p* process: Responsible for the production of neutron-deficient stable nuclei that cannot be produced by the *s* or *r* processes. It is mainly governed by the photodisintegration of *s*- or *r*-produced seed nuclei by high-energy photons causing the emission of nucleons or $\alpha$-particles.
- *i* process: The intermediate neutron-capture process is a nucleosynthesis mechanism that occurs at a neutron density higher than that for the *s* process but lower than for the *r* process and explains certain anomalous abundance patterns.
- CEMP-r/s: Carbon-enhanced metal-poor stars with abundance patterns initially associated with only the *s* and *r* processes.
- AGB: Asymptotic Giant Branch stars represent the late evolutionary stages of low- and intermediate-mass stars (M $\leq$ 8 $M_\odot$). AGB stars are composed of an inert C-O core surrounded by an inner He-burning shell, an intershell rich in helium and carbon, and an outer hydrogen-burning shell.
- CN: A Compound Nucleus is an unstable nucleus, formed when a projectile particle is absorbed by a target nucleus, that exists for a brief period before decaying.
- NLD: The Nuclear Level Density refers to the number of excited energy levels per unit of energy in an atomic nucleus.
- $\gamma$SF: The $\gamma$-ray Strength Function is a measure of the probability of a nucleus emitting a $\gamma$ ray at a specific excitation energy and describes the distribution of $\gamma$-ray energies.

## Acknowledgements

The authors thank Anish Amarsi, Arthur Choplin, Pavel Denissenkov, Jutta Escher, Terese Hansen, Sebastien Martinet, Marco Pignatari and Paul Woodward for useful discussions and support to the manuscript. This material is based upon work supported by the U.S. Department of Energy, Office of Science, Office of Nuclear Physics under Contract No. DE-AC02-05CH11231 and the U.S. Nuclear Data Program (M.W.) and DE-SC0023633 (S.N.L. and A. S.). S.N.L. and A.S acknowledge support from the National Nuclear Security Administration under Award No. DE-NA0003180 and the Stewardship Science Academic Alliances program through DOE Awards No DOE-DE-NA0003906. S.G. acknowledges financial support from F.R.S.-FNRS (Belgium) under Grant Nr IISN 4.4502.19. F.H. is supported by a Natural Sciences and Engineering Research Council of Canada (NSERC) Discovery Grant and acknowledges support from the NSERC award SAPPJ-797 2021-00032 *Nuclear physics of the dynamic origin of the elements*. A.C.L. acknowledges funding the Research Council of Norway, Project Grant No. 316116, and support from ChETEC-INFRA (EU project no. 101008324). A.C.L. and S.S. acknowledge financial support from the Research Council of Norway through the Norwegian Nuclear Research Centre (project No. 341985). A.S. acknowledges the support of the National Science Foundation grant PHY 2209429.


## Author contributions

The authors contributed equally to all aspects of the article.

## Competing interests

The authors declare no competing interests.

## Publisher's note

Springer Nature remains neutral with regard to jurisdictional claims in published maps and institutional affiliations.

## References


1. Alpher, R. A., Bethe, H. & Gamow, G. The Origin of Chemical Elements. *Phys. Rev.* **73**, 803–804 (1948).
2. Merrill, P. Technetium in the stars. *Science* **115**, 484 (1952).
3. Burbidge, E. M., Burbidge, G. R., Fowler, W. A. & Hoyle, F. Synthesis of the Elements in Stars. *Rev. Mod. Phys.* **29**, 547–650 (1957).
4. Cameron, A. G. W. Nuclear Reactions in Stars and Nucleogenesis. *Pub. Astron. Soc. Pac.* **69**, 201–222 (1957).
5. Käppeler, F., Gallino, R., Bisterzo, S. & Aoki, W. The *s* process: Nuclear physics, stellar models, and observations. *Rev. Mod. Phys.* **83**, 157–193 (2011).
6. Arnould, M., Goriely, S. & Takahashi, K. The r-process of stellar nucleosynthesis: Astrophysics and nuclear physics achievements and mysteries. *Phys. Rep.* **450**, 97–213 (2007).
7. Horowitz, C. J. *et al.* r-process nucleosynthesis: connecting rare-isotope beam facilities with the cosmos. *J. Phys. G: Nucl. Part. Phys.* **46**, 083001 (2019).
8. Cowan, J. J. *et al.* Origin of the heaviest elements: The rapid neutron-capture process. *Rev. Mod. Phys.* **93**, 015002 (2021).
9. Arnould, M. & Goriely, S. The p-process of stellar nucleosynthesis: Astrophysics and nuclear physics status. *Phys. Rep.* **384**, 1–84 (2003).
10. Rauscher, T. *et al.* Constraining the astrophysical origin of the p-nuclei through nuclear physics and meteoritic data. *Rep. Prog. Phys.* **76**, 066201 (2013).
11. Cowan, J. J. & Rose, W. K. Production of $^{14}$C and neutrons in red giants. *The Astrophys. J.* **212**, 149–158 (1977).
12. Malaney, R. A. Neutron synthesis in AGB and post-AGB stars of low mass. *Mon. Notices Royal Astron. Soc.* **223**, 683–707 (1986).
13. Jorissen, A. & Arnould, M. Proton mixing in He-rich layers. *Astron. & Astrophys.* **221**, 161–176 (1989).
14. Herwig, F. Evolution of Asymptotic Giant Branch Stars. *Annu. Rev. Astron Astrophys.* **43**, 435–479 (2005).
15. Werner, K. & Herwig, F. The Elemental Abundances in Bare Planetary Nebula Central Stars and the Shell Burning in AGB Stars. *Publ. Astron. Soc. Pac.* **118**, 183–204 (2006).

**16.** Iwamoto, N., Kajino, T., Mathews, G., Fujimoto, M. & Aoki, W. Flash-Driven Convective Mixing in Low-Mass, Metal-deficient Asymptotic Giant Branch Stars: A New Paradigm for Lithium Enrichment and a Possible s-Process. *Astrophys. J.* **602**, 377–387 (2004).

**17.** Cristallo, S. *et al.* Asymptotic-Giant-Branch Models at Very Low Metallicity. *Publ. Astron. Soc. Aust.* **26**, 139–144 (2009).

**18.** Dardelet, L. *et al.* i process and CEMP-s+r stars. In *XIII Nuclei in the Cosmos (NIC XIII)*, 145 (2014).

**19.** Hampel, M., Stancliffe, R. J., Lugaro, M. & Meyer, B. S. The s-process in the Nd-Sm region: Constraints from i-process models and CEMP-r/s stars. *The Astrophys. J.* **831**, 171 (2016).

**20.** Stephens, D. *et al.* 3D1D hydro-nucleosynthesis simulations - I. Advective-reactive post-processing method and its application to H ingestion into He-shell flash convection in rapidly accreting white dwarfs. *Mon. Notices Royal Astron. Soc.* **504**, 744–760 (2021).

**21.** Denissenkov, P. *et al.* The impact of (n, $\gamma$) reaction rate uncertainties of unstable isotopes near N = 50 on the i-process nucleosynthesis in He-shell flash white dwarfs. *J. Phys. G Nucl. Phys.* **45**, 055203 (2018).

**22.** Meyer, B. S., Clayton, D. D. & The, L.-S. Molybdenum and Zirconium Isotopes from a Supernova Neutron Burst. *The Astrophys. J.* **540**, L49–L52 (2000).

**23.** Roederer, I. U., Karakas, A. I., Pignatari, M. & Herwig, F. The Diverse Origins of Neutron-capture Elements in the Metal-poor Star HD 94028: Possible Detection of Products of I-Process Nucleosynthesis. *The Astrophys. J.* **821**, 37 (2016).

**24.** Goriely, S., Siess, L. & Choplin, A. The intermediate neutron capture process II. Nuclear uncertainties. *Astron. & Astrophys.* **654**, A129 (2021).

**25.** Beers, T. C. & Christlieb, N. The Discovery and Analysis of Very Metal-Poor Stars in the Galaxy. *Annu. Rev. Astron. & Astrophys.* **43**, 531–580 (2005).

**26.** Aoki, W., Norris, J. E., Ryan, S. G., Beers, T. C. & Ando, H. Subaru/HDS Study of the Extremely Metal-Poor Star CS 29498-043: Abundance Analysis Details and Comparison with Other Carbon-Rich Objects. *Publ. Astron. Soc. Jpn.* **54**, 933–949 (2002).

**27.** Johnson, J. A. & Bolte, M. The Systematic Behavior of the s- and r-Process Elements in Very Metal-Poor Stars. *The Astrophys. J.* **605**, 462–471 (2004).

**28.** Jonsell, K. *et al.* The Hamburg/ESO R-process enhanced star survey (HERES)-III. HE0338-3945 and the formation of the r-and r/s-stars. *Astron. & Astrophys.* **451**, 651–670 (2006).

**29.** Bisterzo, S., Gallino, R., Straniero, O., Cristallo, S. & Käppeler, F. The s-process in low-metallicity stars – III. Individual analysis of CEMP-s and CEMP-s/r with asymptotic giant branch models. *Mon. Notices Royal Astron. Soc.* **422**, 849–884 (2012).

**30.** Asplund, M., Lambert, D. L., Kipper, T., Pollacco, D. & Shetrone, M. D. The rapid evolution of the born-again giant Sakurai's object. *Astron. & Astrophys.* **343**, 507–518 (1999).

**31.** Herwig, F. *et al.* Convective-reactive proton-$^{12}$C combustion in Sakurai's object (V4334 Sagittarii) and implications for the evolution and yields from the first generations of stars. *The Astrophys. J.* **727**, 89 (2011).

**32.** Fujiya, W., Hoppe, P., Zinner, E., Pignatari, M. & Herwig, F. Evidence for Radiogenic Sulfur-32 in Type AB Presolar Silicon Carbide Grains? *The Astrophys. J.* **776**, L29 (2013).

**33.** Liu, N. *et al.* Isotopic Records in AGB Stars from the Torino Postprocess AGB Model. *The Astrophys. J.* **786**, 66 (2014).

**34.** Lugaro, M. *et al.* Post-AGB stars in the Magellanic Clouds and neutron-capture processes in AGB stars. *Astron. & Astrophys.* **583**, A77 (2015).

**35.** Cseh, B. *et al.* Barium stars as tracers of s-process nucleosynthesis in AGB stars. I. 28 stars with independently derived AGB mass. *Astron. & Astrophys.* **661**, A77 (2022).

**36.** den Hartogh, J. W. *et al.* Barium stars as tracers of s-process nucleosynthesis in AGB stars. II. Using machine learning techniques on 169 stars. *Astron. & Astrophys.* **672**, A143 (2023).

**37.** Világos, B. *et al.* Barium stars as tracers of s-process nucleosynthesis in AGB stars. III. Systematic deviations from the AGB models. *Astron. & Astrophys.* **688**, A164 (2024).

**38.** Roriz, M. P. *et al.* Tungsten in barium stars. *Mon. Notices Royal Astron. Soc.* **528**, 4354–4363 (2024).

**39.** Dorsch, M. *et al.* Heavy-metal enrichment of intermediate He-sdOB stars: the pulsators Feige 46 and LS IV-14°116 revisited. *Astron. Astrophys.* **643**, A22 (2020).

**40.** Battich, T., Miller Bertolami, M. M., Serenelli, A. M., Justham, S. & Weiss, A. A self-synthesized origin for heavy metals in hot subdwarf stars. *Astron. Astrophys.* **680**, L13 (2023).

**41.** Mishenina, T. *et al.* Abundances of neutron-capture elements in stars of the Galactic disk substructures. *Mon. Notices Royal Astron. Soc.* **446**, 3651–3668 (2015).

**42.** Bertolli, M. G., Herwig, F., Pignatari, M. & Kawano, T. Systematic and correlated nuclear uncertainties in the i-process at the neutron shell closure N = 82. *arXiv e-prints* arXiv:1310.4578 (2013).

**43.** Spyrou, A. *et al.* First Study of the $^{139}Ba(n,\gamma)^{140}Ba$ Reaction to Constrain the Conditions for the Astrophysical *i* Process. *Phys. Rev. Lett.* **132**, 202701 (2024).

**44.** Keller, S. C. *et al.* A single low-energy, iron-poor supernova as the source of metals in the star SMSS J031300.36-670839.3. *Nature* **506**, 463–466 (2014).

**45.** Clarkson, O., Herwig, F. & Pignatari, M. Nucleosynthesis in the first stars studied with a new, accurate neutron capture rate for $^{13}C(\alpha,n)^{16}O$. *Mon. Notices Royal Astron. Soc.* **474**, L37–L41 (2018).

**46.** McKay, J. E., Denissenkov, P. A., Herwig, F., Perdikakis, G. & Schatz, H. The impact of $(n,\gamma)$ reaction rate uncertainties on the predicted abundances of i-process elements with $32 \leq Z \leq 48$ in the metal-poor star HD94028. *Mon. Notices Royal Astron. Soc.* **491**, 5179–5187 (2019).

**47.** Alencastro Puls, A. *et al.* Chemical Evolution of R-process Elements in Stars (CERES): IV. An observational run-up of the third r-process peak with Hf, Os, Ir, and Pt. *Astron. & Astrophys.* **693**, A294 (2025).

**48.** Côté, B. *et al.* Neutron Star Mergers Might Not Be the Only Source of r-process Elements in the Milky Way. *The Astrophys. J.* **875**, 106 (2019).

**49.** Masseron, T. *et al.* A holistic approach to carbon-enhanced metal-poor stars. *Astron. & Astrophys.* **509**, A93 (2010).

**50.** Hansen, C. J. *et al.* Abundances and kinematics of carbon-enhanced metal-poor stars in the Galactic halo. A new classification scheme based on Sr and Ba. *Astron. & Astrophys.* **623**, A128 (2019).

**51.** Karinkuzhi, D. *et al.* Low-mass low-metallicity AGB stars as an efficient i-process site explaining CEMP-rs stars. *Astron. & Astrophys.* **645**, A61 (2021).

**52.** Hansen, T. T. *et al.* The role of binaries in the enrichment of the early Galactic halo. III. Carbon-enhanced metal-poor stars - CEMP-s stars. *Astron. & Astrophys.* **588**, A3 (2016).

**53.** Vassh, N. *et al.* Classifying metal-poor stars with machine learning using nucleosynthesis calculations (2025). 2505.14563.

**54.** Mashonkina, L. & Christlieb, N. The Hamburg/ESO R-process Enhanced Star survey (HERES). IX. Constraining pure r-process Ba/Eu abundance ratio from observations of r-II stars. *Astron. & Astrophys.* **565**, A123 (2014).

**55.** Magain, P. & Zhao, G. Barium isotopes in the very metal-poor star HD 140283. *Astron. & Astrophys.* **268**, L27 (1993).

**56.** Lambert, D. L. & Allende Prieto, C. The isotopic mixture of barium in the metal-poor subgiant HD 140283. *Mon. Not. Roy. Astron. Soc.* **335**, 325–334 (2002).

**57.** Gallagher, A. J., Ludwig, H. G., Ryan, S. G. & Aoki, W. A three-dimensional hydrodynamical line profile analysis of iron lines and barium isotopes in HD 140283. *Astron. & Astrophys.* **579**, A94 (2015).

**58.** Van Eck, S. *et al.* From the s-Process to the i-Process: A New Perspective on the Chemical Enrichment of Extrinsic Stars. *Galaxies* **12**, 89 (2024).

**59.** Mashonkina, L. I. & Belyaev, A. K. Even-to-Odd Barium Isotope Ratio in Selected Galactic Halo Stars. *Astron. Lett.* **45**, 341–353 (2019).

**60.** Gallagher, A. J. *et al.* Observational constraints on the origin of the elements. II. 3D non-LTE formation of Ba II lines in the solar atmosphere. *Astron. & Astrophys.* **634**, A55 (2020).

**61.** Bergemann, M., Lind, K., Collet, R., Magic, Z. & Asplund, M. Non-LTE line formation of Fe in late-type stars - I. Standard stars with 1D and <3D> model atmospheres. *Mon. Not. Roy. Astron. Soc.* **427**, 27–49 (2012).

**62.** Lind, K. & Amarsi, A. M. Three-Dimensional Nonlocal Thermodynamic Equilibrium Abundance Analyses of Late-Type Stars. *Annu. Rev. Astron. Astrophys.* **62**, 475–527 (2024).

**63.** Jofré, P., Heiter, U. & Soubiran, C. Accuracy and Precision of Industrial Stellar Abundances. *Annu. Rev. Astron. Astrophys.* **57**, 571–616 (2019).

**64.** Buder, S. *et al.* The GALAH+ survey: Third data release. *Mon. Notices Royal Astron. Soc.* **506**, 150–201 (2021).

**65.** Abdurro'uf *et al.* The Seventeenth Data Release of the Sloan Digital Sky Surveys: Complete Release of MaNGA, MaStar, and APOGEE-2 Data. **259**, 35 (2022).

**66.** de Jong, R. S. *et al.* 4MOST: Project overview and information for the First Call for Proposals. *The Messenger* **175**, 3–11 (2019).

**67.** Jin, S. *et al.* The wide-field, multiplexed, spectroscopic facility WEAVE: Survey design, overview, and simulated implementation. **530**, 2688–2730 (2024).

**68.** Nissen, P. E. & Gustafsson, B. High-precision stellar abundances of the elements: methods and applications. **26**, 6 (2018).

**69.** Herwig, F., Blöcker, T., Langer, N. & Driebe, T. On the formation of hydrogen-deficient post-AGB stars. *Astron. & Astrophys.* **349**, L5–L8 (1999).

**70.** Choplin, A., Siess, L. & Goriely, S. The intermediate neutron capture process III. The i-process in AGB stars of different masses and metallicities without overshoot. *Astron. Astrophys.* **667**, A155 (2022).

**71.** Herwig, F., Woodward, P. R., Lin, P.-H., Knox, M. & Fryer, C. Global Non-spherical Oscillations in Three-dimensional $4\pi$ Simulations of the H-ingestion Flash. *The Astrophys. J. Lett.* **792**, L3 (2014).

**72.** Hampel, M., Karakas, A. I., Stancliffe, R. J., Meyer, B. S. & Lugaro, M. Learning about the Intermediate Neutron-capture Process from Lead Abundances. *The Astrophys. J.* **887**, 11 (2019).

**73.** Denissenkov, P. A., Herwig, F., Perdikakis, G. & Schatz, H. The impact of (n,$\gamma$) reaction rate uncertainties of unstable isotopes on the i-process nucleosynthesis of the elements from Ba to W. *Mon. Notices Royal Astron. Soc.* **503**, 3913–3925 (2021).

**74.** Choplin, A., Goriely, S. & Siess, L. Synthesis of thorium and uranium in asymptotic giant branch stars. *Astron. & Astrophys.* **667**, L13 (2022).

**75.** Choplin, A., Siess, L., Goriely, S. & Martinet, S. The intermediate neutron capture process V. The i-process in AGB stars with overshoot. *Astron. Astrophys.* **684**, A206 (2024).

**76.** Denissenkov, P. A. *et al.* I-process Nucleosynthesis and Mass Retention Efficiency in He-shell Flash Evolution of Rapidly Accreting White Dwarfs. *The Astrophys. J. Lett.* **834**, L10 (2017).

**77.** Denissenkov, P. A. *et al.* The i-process yields of rapidly accreting white dwarfs from multicycle He-shell flash stellar evolution models with mixing parametrizations from 3D hydrodynamics simulations. *Mon. Notices Royal Astron. Soc.* **488**, 4258–4270 (2019).

**78.** Fujimoto, M. Y., Ikeda, Y. & Iben, I., Jr. The Origin of Extremely Metal-poor Carbon Stars and the Search for Population III. *Astrophys. Journal, Lett.* **529**, L25–L28 (2000).

**79.** Chieffi, A., Dominguez, I., Limongi, M. & Staniero, O. Evolution and Nucleosynthesis of Zero-Metal Intermediate-Mass Stars. *Astrophys. J.* **553**, 1159–1174 (2001).

**80.** Siess, L., Livio, M. & Lattanzio, J. Structure, Evolution, and Nucleosynthesis of Primordial Stars. *Astrophys. J.* **570**, 329–343 (2002).

**81.** Suda, T. & Fujimoto, M. Y. Evolution of low- and intermediate-mass stars with [Fe/H] <= - 2.5. *Mon. Notices RAS* **405**, 177–193 (2010).

**82.** Cristallo, S., Karinkuzhi, D., Goswami, A., Piersanti, L. & Gobrecht, D. Constraints of the Physics of Low-mass AGB Stars from CH and CEMP Stars. *Astrophys. J.* **833**, 181 (2016).

**83.** Choplin, A., Siess, L. & Goriely, S. The intermediate neutron capture process I. Development of the i-process in low-metallicity low-mass AGB stars. *Astron. & Astrophys.* **648**, A119 (2021).

**84.** Schlattl, H., Cassisi, S., Salaris, M. & Weiss, A. On the Helium Flash in Low-Mass Population III Red Giant Stars. *Astrophys. J.* **559**, 1082–1093 (2001).

**85.** Campbell, S. W., Lugaro, M. & Karakas, A. I. Evolution and nucleosynthesis of extremely metal-poor and metal-free low- and intermediate-mass stars. II. s-process nucleosynthesis during the core He flash. *Astron. Astrophys.* **522**, L6 (2010).

**86.** Cruz, M. A., Serenelli, A. & Weiss, A. S-process in extremely metal-poor, low-mass stars. *Astron. Astrophys.* **559**, A4 (2013).

**87.** Jones, S. *et al.* H ingestion into He-burning convection zones in super-AGB stellar models as a potential site for intermediate neutron-density nucleosynthesis. *Mon. Notices Royal Astron. Soc.* **455**, 3848–3863 (2016).

**88.** Siess, L. Evolution of massive AGB stars. II. model properties at non-solar metallicity and the fate of Super-AGB stars. *Astron. Astrophys.* **476**, 893–909 (2007).

**89.** Banerjee, P., Qian, Y.-Z. & Heger, A. New Neutron-capture Site in Massive Pop III and Pop II Stars as a Source for Heavy Elements in the Early Galaxy. *Astrophys. J.* **865**, 120 (2018).

**90.** Clarkson, O., Herwig, F. & Pignatari, M. Pop III i-process nucleosynthesis and the elemental abundances of SMSS J0313-6708 and the most iron-poor stars. *Mon. Not. Roy. Astron. Soc.* **474**, L37–L41 (2018).

**91.** Clarkson, O. & Herwig, F. Convective H-He Interactions in Massive Population III Stellar Evolution Models. *Mon. Not. Roy. Astron. Soc.* **500**, 2685–2703 (2021).

**92.** Martinet, S., Choplin, A., Goriely, S. & Siess, L. The intermediate neutron capture process IV. Impact of nuclear model and parameter uncertainties. *Astron. & Astrophys.* **684**, A8 (2024).

**93.** Hauser, W. & Feshbach, H. The inelastic scattering of neutrons. *Phys. Rev.* **87**, 366–373 (1952).

**94.** Bartholomew, G. A., Earle, E. D., Ferguson, A. J., Knowles, J. W. & Lone, M. A. *Gamma-Ray Strength Functions*, 229–324 (Springer US, Boston, MA, 1973).

**95.** Wiedeking, M. & Goriely, S. Photon strength functions and nuclear level densities: invaluable input for nucleosynthesis. *Phil. Trans. R. Soc. A.* **382**, 20230125 (2024).

**96.** Capote, R. *et al.* Reference Input Parameter Library (RIPL-3). *Nucl. Data Sheets* **110**, 3107–3214 (2009).

**97.** Bethe, H. An Attempt to Calculate the Number of Energy Levels of a Heavy Nucleus. *Phys. Rev.* **50**, 332–341 (1936).

**98.** Ericson, T. A statistical analysis of excited nuclear states. *Nucl. Phys.* **11**, 481–491 (1959).

**99.** Gilbert, A. & Cameron, A. G. W. A composite nuclear-level density formula with shell corrections. *Can. J. Phys.* **43**, 1446–1496 (1965).

**100.** Demetriou, P. & Goriely, S. Microscopic nuclear level densities for practical applications. *Nucl. Phys. A* **695**, 95–108 (2001).

**101.** Goriely, S., Hilaire, S. & Koning, A. J. Improved predictions of nuclear reaction rates with the TALYS reaction code for astrophysical applications. *Astron. & Astrophys.* **487**, 767–774 (2008).

**102.** Hilaire, S., Girod, M., Goriely, S. & Koning, A. J. Temperature-dependent combinatorial level densities with the D1M Gogny force. *Phys. Rev. C* **86**, 064317 (2012).

**103.** Døssing, T. & Aberg, S. Collective enhancements in nuclear level densities. *Eur. Phys. J. A* **55**, 249 (2019).

**104.** Zelevinsky, V. & Karampagia, S. Nuclear level density and related physics. *EPJ Web Conf.* **194**, 01001 (2018).

**105.** Alhassid, Y. The shell model Monte Carlo approach to level densities: Recent developments and perspectives. *Eur. Phys. J. A* **51**, 171 (2015).

**106.** Wang, J., Dutta, S., Wang, L.-J. & Sun, Y. Projected shell model description of nuclear level density: Collective, pair-breaking, and multiquasiparticle regimes in even-even nuclei. *Phys. Rev. C* **108**, 034309 (2023).

**107.** Hilaire, S., Goriely, S., Péru, S. & Gosselin, G. A new approach to nuclear level densities: The QRPA plus boson expansion. *Phys. Lett. B* **843**, 137989 (2023).

**108.** Kadmenskii, S., Markushev, V. & Furmann, V. Radiative Strength Functions and the Problem of Enhanced Radiative Capture in the Region of Superfluid Nuclei. *Sov. J. Nucl. Phys.* **37**, 165–168 (1983).

**109.** Mercenne, A., Fanto, P., Ryssens, W. & Alhassid, Y. Magnetic dipole $\gamma$-ray strength functions in the crossover from spherical to deformed neodymium isotopes. *Phys. Rev. C* **110**, 054313 (2024).

**110.** Chen, F.-Q., Niu, Y. F., Sun, Y. & Wiedeking, M. Origin of the Low-Energy Enhancement of the $\gamma$-Ray Strength Function. *Phys. Rev. Lett.* **134**, 082502 (2025).

**111.** Goriely, S. *et al.* Reference Database for Photon Strength Functions. *Eur. Phys. J. A* **55**, 172 (2019).

**112.** Daoutidis, I. & Goriely, S. Large-scale continuum random-phase approximation predictions of dipole strength for astrophysical applications. *Phys. Rev. C* **86**, 034328 (2012).

**113.** Egorova, I. A. & Litvinova, E. Electric dipole response of neutron-rich calcium isotopes in relativistic quasiparticle time blocking approximation. *Phys. Rev. C* **94**, 034322 (2016).

**114.** Voinov, A. *et al.* Large Enhancement of Radiative Strength for Soft Transitions in the Quasicontinuum. *Phys. Rev. Lett.* **93**, 142504 (2004).

**115.** Wiedeking, M. *et al.* Low-Energy Enhancement in the Photon Strength of $^{95}$Mo. *Phys. Rev. Lett.* **108**, 162503 (2012).

**116.** Larsen, A. C. *et al.* Low-energy enhancement and fluctuations of $\gamma$-ray strength functions in $^{56,57}$Fe: test of the Brink–Axel hypothesis. *J. Phys. G: Nucl. Part. Phys.* **44**, 064005 (2017).

**117.** Jones, M. D. *et al.* Examination of the low-energy enhancement of the $\gamma$-ray strength function of $^{56}$Fe. *Phys. Rev. C* **97**, 024327 (2018).

**118.** Litvinova, E. & Belov, N. Low-energy limit of the radiative dipole strength in nuclei. *Phys. Rev. C* **88**, 031302(R) (2013).

**119.** Schwengner, R., Frauendorf, S. & Larsen, A. C. Low-Energy Enhancement of Magnetic Dipole Radiation. *Phys. Rev. Lett.* **111**, 232504 (2013).

**120.** Schwengner, R., Frauendorf, S. & Brown, B. A. Low-Energy Magnetic Dipole Radiation in Open-Shell Nuclei. *Phys. Rev. Lett.* **118**, 092502 (2017).

**121.** Frauendorf, S. & Schwengner, R. Evolution of low-lying M1 modes in germanium isotopes. *Phys. Rev. C* **105**, 034335 (2022).

**122.** Goriely, S., Hilaire, S., Péru, S. & Sieja, K. Gogny-HFB+QRPA dipole strength function and its application to radiative nucleon capture cross section. *Phys. Rev. C* **98**, 014327 (2018).

**123.** Zeiser, F. *et al.* The $\gamma$-ray energy response of the Oslo Scintillator Array OSCAR. *Nucl. Instruments Methods Phys. Res. Sect. A: Accel. Spectrometers, Detect. Assoc. Equip.* **985**, 164678 (2021).

**124.** Guttormsen, M., Bürger, A., Hansen, T. & Lietaer, N. The SiRi particle-telescope system. *Nucl. Instruments Methods Phys. Res. Sect. A: Accel. Spectrometers, Detect. Assoc. Equip.* **648**, 168–173 (2011).

**125.** Cramer, J. D. & Britt, H. C. Neutron Fission Cross Sections for 231Th, 233Th, 235U, 237U, 239U, 241Pu, and 243Pu from 0.5 to 2.25 MeV Using (t, pf) Reactions. *Nucl. Sci. Eng.* **41**, 177–187 (1970).

**126.** Escher, J. E. *et al.* Compound-nuclear reaction cross sections from surrogate measurements. *Rev. Mod. Phys.* **84**, 353–397 (2012).

**127.** Wilson, J. N. *et al.* Indirect $(n,\gamma)$ cross sections of thorium cycle nuclei using the surrogate method. *Phys. Rev. C* **85**, 034607 (2012).

**128.** Potel, G., Nunes, F. M. & Thompson, I. J. Establishing a theory for deuteron-induced surrogate reactions. *Phys. Rev. C* **92**, 034611 (2015).

**129.** Ducasse, Q. *et al.* Investigation of the $^{238}$U$(d,p)$ surrogate reaction via the simultaneous measurement of $\gamma$-decay and fission probabilities. *Phys. Rev. C* **94**, 024614 (2016).

**130.** Escher, J. E. *et al.* Constraining Neutron Capture Cross Sections for Unstable Nuclei with Surrogate Reaction Data and Theory. *Phys. Rev. Lett.* **121**, 052501 (2018).

**131.** Ratkiewicz, A. *et al.* Towards Neutron Capture on Exotic Nuclei: Demonstrating $(d,p\gamma)$ as a Surrogate Reaction for $(n,\gamma)$. *Phys. Rev. Lett.* **122**, 052502 (2019).

**132.** Escher, Jutta E. The Surrogate Nuclear Reaction Method: Concept, recent advances, and new opportunities. *EPJ Web Conf.* **322**, 03001 (2025).

**133.** Allmond, J. M. *et al.* Relative $^{235}$U$(n,\gamma)$ and $(n,f)$ cross sections from $^{235}$U$(d,p\gamma)$ and $(d,pf)$. *Phys. Rev. C* **79**, 054610 (2009).

**134.** Hatarik, R. *et al.* Benchmarking a surrogate reaction for neutron capture. *Phys. Rev. C* **81**, 011602 (2010).

**135.** Yan, S. Q. *et al.* Examination of the surrogate ratio method for the determination of the $^{93}$Zr$(n,\gamma)$ $^{94}$Zr cross section with $^{90,92}$Zr($^{18}$O,$^{16}$O) $^{92,94}$Zr reactions. *Phys. Rev. C* **94**, 015804 (2016).

**136.** Yan, S. Q. *et al.* The $^{95}$Zr(n,$\gamma$)$^{96}$Zr Cross Section from the Surrogate Ratio Method and Its Effect on s-process Nucleosynthesis. *The Astrophys. J.* **848**, 98 (2017).

**137.** Yan, S. Q. *et al.* The $^{59}$Fe(n,$\gamma$)$^{60}$Fe Cross Section from the Surrogate Ratio Method and Its Effect on the 60Fe Nucleosynthesis". *The Astrophys. J.* **919**, 84 (2021).

**138.** Rekstad, J. *et al.* A study of nuclear structure at high energy and low spin. *Phys. Scripta* **T5**, 45–50 (1983).

**139.** Bergholt, L., Guttormsen, M., Rekstad, J. & Tveter, T. On the relation between the statistical gamma-decay and the level density in 162Dy. *Nucl. Phys. A* **589**, 249–266 (1995).

**140.** Tveter, T. S., Bergholt, L., Guttormsen, M., Melby, E. & Rekstad, J. Observation of Fine Structure in Nuclear Level Densities and $\gamma$-Ray Strength Functions. *Phys. Rev. Lett.* **77**, 2404 (1996).

**141.** Schiller, A. *et al.* Extraction of level density and gamma strength function from primary gamma spectra . *Nucl. Instruments Methods Phys. Res. Sect. A, Accel. Spectrometers, Detect. Assoc. Equip.* **447**, 498–511 (2000).

**142.** Markova, M. *et al.* Nuclear level densities and $\gamma$-ray strength functions of $^{111,112,113}$Sn isotopes studied with the Oslo method. *Phys. Rev. C* **108**, 014315 (2023).

**143.** Guttormsen, M., Tveter, T., Bergholt, L., Ingebretsen, F. & Rekstad, J. The unfolding of continuum gamma-ray spectra. *Nucl. Instruments Methods Phys. Res. Sect. A, Accel. Spectrometers, Detect. Assoc. Equip.* **374**, 371–376 (1996).

**144.** Guttormsen, M., Ramsøy, T. & Rekstad, J. The first generation of gamma-rays from hot nuclei. *Nucl. Instruments Methods Phys. Res. Sect. A: Accel. Spectrometers, Detect. Assoc. Equip.* **255**, 518–523 (1987).

**145.** Brink, D. M. *Some aspects of the interaction of light with matter*. Ph.D. thesis, Oxford University (1955).

**146.** Axel, P. Electric dipole ground-state transition. *Phys. Rev.* **126**, 671–683 (1962).

**147.** Pogliano, F. *et al.* Indirect measurement of the $(n,\gamma)^{127}$Sb cross section. *Phys. Rev. C* **106**, 015804 (2022).

**148.** Ingeberg, V. W. *et al.* First application of the Oslo method in inverse kinematics. *Eur. Phys. J. A* **56**, 68 (2020).

**149.** Ingeberg, V. W. *et al.* Nuclear level density and $\gamma$-ray strength function of $^{67}$Ni and the impact on the *i* process. *Phys. Rev. C* **111**, 015803 (2025).

**150.** Spyrou, A. *et al.* Novel technique for Constraining r-Process (n, $\gamma$) Reaction Rates. *Phys. Rev. Lett.* **113**, 232502 (2014).

**151.** Liddick, S. *et al.* Experimental Neutron Capture Rate Constraint Far from Stability. *Phys. Rev. Lett.* **116**, 242502 (2016).

**152.** Liddick, S. N. *et al.* Benchmarking the extraction of statistical neutron capture cross sections on short-lived nuclei for applications using the $\beta$-Oslo method. *Phys. Rev. C* **100**, 024624 (2019).

**153.** Wiedeking, M. *et al.* Independent normalization for $\gamma$-ray strength functions: The shape method. *Phys. Rev. C* **104**, 014311 (2021).

**154.** Mücher, D. *et al.* Extracting model-independent nuclear level densities away from stability. *Phys. Rev. C* **107**, L011602 (2023).

**155.** Sweet, A. *et al.* Nuclear level density and $\gamma$-decay strength of $^{93}$Sr. *Phys. Rev. C* **109**, 054305 (2024).

**156.** Klein, M. J. Principle of Detailed Balance. *Phys. Rev.* **97**, 1446 (1955).

**157.** Rossi, D. M. *et al.* Measurement of the Dipole Polarizability of the Unstable Neutron-Rich Nucleus $^{68}$Ni. *Phys. Rev. Lett.* **111**, 242503 (2013).

**158.** Wieland, O. *et al.* Low-lying dipole response in the unstable $^{70}$Ni nucleus. *Phys. Rev. C* **98**, 064313 (2018).

**159.** Adrich, P. *et al.* Evidence for Pygmy and Giant Dipole Resonances in $^{130}$Sn and $^{132}$Sn. *Phys. Rev. Lett.* **95**, 132501 (2005).

**160.** Ershova, O. *et al.* Coulomb dissociation reactions on Mo isotopes for astrophysics applications. In *Proceedings of the 11th Symposium on Nuclei in the Cosmos (NIC XI)*, vol. 100, 232 (2011).

**161.** Takeuchi, S. *et al.* Coulomb breakup reactions of 93,94Zr in inverse kinematics. *Prog. Theor. Exp. Phys.* **2019**, 013D02 (2019).

**162.** Avigo, R. *et al.* Low-lying electric dipole $\gamma$-continuum for the unstable 62,64Fe nuclei: Strength evolution with neutron number. *Phys. Lett. B* **811**, 135951 (2020).

**163.** Vonach, H. Extraction of level density information from non-resonance reactions. In Bhat, M. R. (ed.) *Proceedings of the IAEA Advisory Group Meeting on Basic and Applied Problems of Nuclear Level Densities*, BNL Report No. BNL-NCS-51694, 247–290 (Brookhaven National Laboratory, Upton, Long Island, New York 11973, 1983).

**164.** Voinov, A. V. *et al.* Reduction of the neutron imaginary potential off the stability line and its possible impact on neutron capture rates. *Phys. Rev. C* **104**, 015805 (2021).

**165.** Soltesz, D. *et al.* Determination of the $^{60}$Zn level density from neutron evaporation spectra. *Phys. Rev. C* **103**, 015802 (2021).

**166.** Voinov, A. V. *et al.* Level densities for $^{69,71}$Ga nuclei using a particle-evaporation technique. *Phys. Rev. C* **109**, 054601 (2024).

**167.** Johnson, J. A. & Bolte, M. The s-Process in Metal-Poor Stars: Abundances for 22 Neutron-Capture Elements in CS 31062-050. *The Astrophys. J.* **605**, 462–471 (2004).

**168.** Aoki, W. *et al.* Carbon-enhanced Metal-poor Stars: Osmium and Iridium Abundances in the Neutron-Capture-enhanced Subgiants CS 31062-050 and LP 625-44*. *The Astrophys. J. Lett.* **650**, L127–L130 (2006).

**169.** Lai, D. K., Johnson, J. A., Bolte, M. & Lucatello, S. Carbon and Strontium Abundances of Metal-poor Stars. *The Astrophys. J.* **667**, 1185–1195 (2007).

**170.** Gull, M. *et al.* The R-Process Alliance: Discovery of the First Metal-poor Star with a Combined r- and s-process Element Signature. *The Astrophys. J.* **862**, 174 (2018).

**171.** Vassh, N. *et al.* Thallium-208: A Beacon of In Situ Neutron Capture Nucleosynthesis. *Phys. Rev. Lett.* **132**, 052701 (2024).